Graduate School of Frontier Sciences, The University of Tokyo
Natural Environmental Studies, Division of Environmental Studies
Marine Environmental Dynamics

School Year 2022
Master Thesis

Spread of river water influenced by wind in Otsuchi Bay
大槌湾において風の影響を受けて拡がる河川系水

Submission: Aug. 24, 2022
for completion in Sep. 2022

Supervisor: Associate Professor Kiyoshi Tanaka

47-206771
Yoojun Kim (金 裕竣)

Contents

Abstract

1. Introduction

Sanriku ria coast in the northeastern part of Japan is characterized by its complex topography including a continental shelf, slope, and saw-blade-like coastline, where various water masses, such as Tsugaru Warm Current Water, Oyashio Water, and occasionally even Kuroshio Water meet. Because of these characteristics, the Sanriku region is one of the highest productivity areas in Japan. Indeed approximately 20% of aquaculture fishery products in Japan are produced in this region.

Otsuchi Bay is one of the bays on the Sanriku ria coast (Fig.1-1). The bay is open to the north Pacific. The size of the bay is approximately 8 km long and 2 km wide, with a sloping bottom topography that deepened down to 70 m depth at the bay mouth. Three rivers (Otsuchi, Kozuchi, and Unosumai) flow into the bay, and their discharged volume varies from 3 to 35 $m^3 s^{-1}$ (Anbo et al. 2005).

This bay is also characterized by the aquaculture of oysters, seaweed, and so on. The productivity of aquaculture is greatly affected by circulation because it is influenced by the coastal material circulation, which provides nutrients and affects the plankton blooming. (Furuya et al. 1993; Kawamiya et al. 1996; Kishi et al. 2003). According to Furuya et al. (1993), strong westerly wind reinforces the estuary circulation and shifts the plankton blooming toward offshore. On the other hand, calm weather (i.e., weak westerly wind) supports plankton blooming inside the bay. In addition to that, Kawamiya et al. (1996) and Kishi et al. (2003) performed numerical experiments on the phytoplankton blooming with physical-biology coupled models. They pointed out the role of westerly wind and river water on the estuary-like circulation and consequent material circulations. However, they mainly focused on the vertical circulation, which is related to plankton blooms, rather than the horizontal distribution of the river water. Therefore, it is still important to elucidate the circulation in the bay.

According to previous studies (Ishizu et al. 2017; Otobe et al. 2009; Tanaka et al. 2017), Pacific water such as Tsugaru Warm Current Water or Oyashio Water intrudes the bay. Otobe et al. (2009) mentioned that there is the possibility that seasonal wind (northwesterly) strengthens the estuary circulation. Moreover, according to Isuizu et al. (2017), wind stress is closely related to the Oyashio Water intrusion. Therefore, the wind is an important factor in circulation.

In the bay, it has often been observed that low salinity water generally exists on the southern coast, forming a meridionally positive salinity gradient pattern (north high saline, south low saline). This pattern appears to be consistent with that obtained by idealized theoretical studies considering the effect of the Earth rotation (Coriolis force) in the northern hemisphere (e.g., Minato,1983; Yankovsky and Chapman, 1997), where low-salinity water tends to flow with the coast to the right.

This phenomenon is related to the internal Rossby deformation radius, which is the length scale of geostrophic adjustment: The process where an initially unbalanced state naturally evolves toward a state of geostrophic balance where only Coriolis force and pressure gradient force balance each other in the horizontal components of the fluid momentum equation (e.g., Vallis, 2006). That is, the river water is generally confined within the internal Rossby deformation radius from the coast. Therefore, the river water spread is affected by Earth's rotation.

There were several studies that investigated river water spread in Otsuchi Bay (Masunaga et al. 2016; Sasmal et al. 2018). However, three-dimensional patterns of the circulation under the influence of the Earth's rotation have not been investigated thoroughly.

In the study of Sakamoto et al. (2017) with realistic topography and nested-grid ocean general circulation model, Pacific water intrusion and anticlockwise circulation similar to observed data by Otobe et al. (2009) were successfully reproduced. However, the circulation pattern in winter disagreed at some points with observed data by Otobe et al. (2009) and suggested it as a remained future work.

In their study (Sakamoto et al. 2017), the internal Rossby deformation radii variate from 1000 m to 2000 m with the season. With their reproduced Pacific water intrusion and anticlockwise circulation, low salinity water generally exists on the southern coast, forming the meridionally positive salinity gradient pattern, which is consistent with idealized theoretical studies (e.g., Minato,1983). However, in Otsuchi Bay, the observed internal Rossby deformation radius variates by time and place from 300 m to 4980 m (Ishizu et al. 2017; Otobe et al. 2009; Tanaka et al. 2017), which were bigger or smaller compared to the width of the bay. This implies the possibility that various river water spread patterns could exist, rather than the positive salinity gradient pattern. Therefore, in this study, we conducted both analysis of high-resolution observation data that has never been seen before and numerical experiments under conditions that have not been examined yet, to investigate river water spread in the bay with the effect of wind and the Earth's rotation.

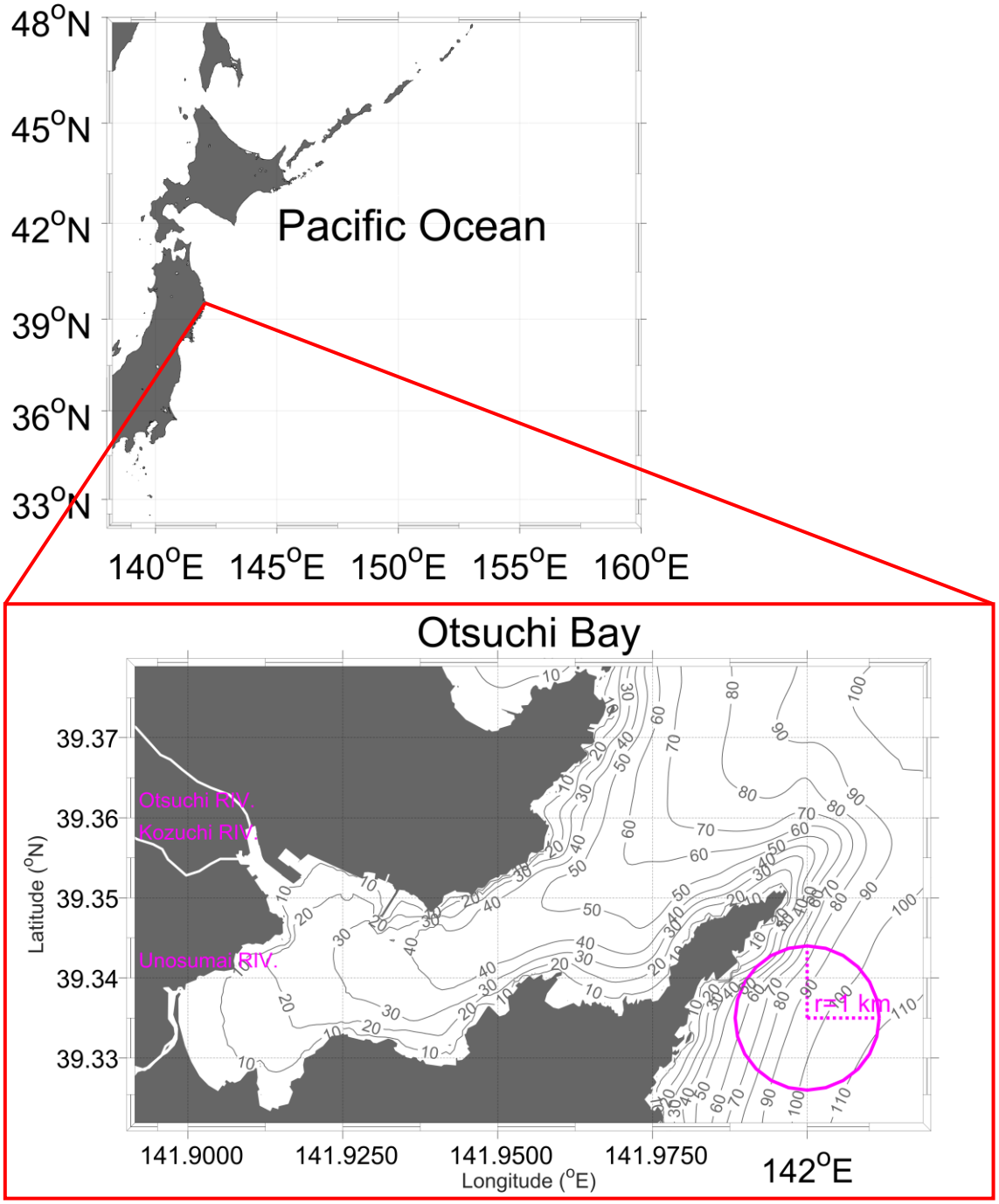

Fig.1-1, Location and bottom topography of Otsuchi Bay. Magenta circle with radius 1 km shows relative scale of the bay.

2. Materials and Methods

2.1 Ocean observed data and analysis

We used the high-resolution of Conductivity-Temperature-Depth (CTD) observed data which had been obtained in Otsuchi Bay: They were obtained about monthly at 44 stations from 1990 to 1991, 42 stations from 2014 to 2015, and 9 stations from 2018 to 2019 (Fig. 2.1-1). Detailed information is given in the appendix (A.2.1-1). In the coastal regions where the high-salinity outer (Pacific) water and the low-salinity river water meet, the salinity is the most distinct physical variable in understanding the circulation. Since we aim to elucidate the circulation patterns in the bay that are formed by the river water spread, we focused on the distribution of the sea surface salinity and it was defined by depth-averaged salinity within $1-3$ m, on the basis of vertical profile of the density (Fig.2.1-2). Although spatial and temporal distributions of observed stations were slightly different by observed year, we utilized as many observations as possible to understand the statistical relationship of the bay which would be discussed in the following paragraph.

Objective analysis, such as optimal interpolation, statistical interpolation, and kriging, is one of the interpolation methods that utilize statistical relationships among observed data. The interpolation gives regularly-gridded data which enables objective mapping of the observed data. What is important is that we should select the appropriate method to minimize the interpolation errors. In this study, we applied the Kuragano and Kamachi (2000) method, in which they utilized an anisotropic (ellipse-shaped) correlation function to take the anisotropic spatial distribution of the observed variable into consideration. Indeed, statistical relationship has directional dependency (anisotropic) in Otsuchi Bay: The correlations among sea surface salinity were higher in the along-bay directions compared to the cross-bay directions (Fig. 2.1-3). Following the method of Kuragano and Kamachi (2000) with some modifications, the observed correlations between pairs of stations were fitted to the observed correlation function (μ^o),

$$\mu^o = e^{\alpha_1 x^2+\alpha_2 y^2+\alpha_3 xy+\alpha_4} \quad , \tag{2.1.1}$$

where, x and y are longitudinal distance and latitudinal distances between those stations (Fig.2.1-4). The last coefficient α_4 is related to signal to noise ratio (λ), which is

$$\frac{1}{\lambda} = \frac{\sigma^t}{\sigma^e} = \sqrt{\frac{e^{\alpha_4}}{1-e^{\alpha_4}}} \ . \tag{2.1.2}$$

The coefficients, α_1, α_2, α_3, and α_4, were estimated to be -0.037, -0.062, 0.067, and -0.150,

respectively (Fig.2.1-5). Detailed procedures of the objective analysis were done referred to Bretherton et al. (1976) and Mizuno (1995), which is given in the appendix (A.2.1-2). Also, comparison of objective analysis methods between anisotropic (Kuragano and Kamachi 2000) and isotropic is also given in the appendix (A.2.1-3).

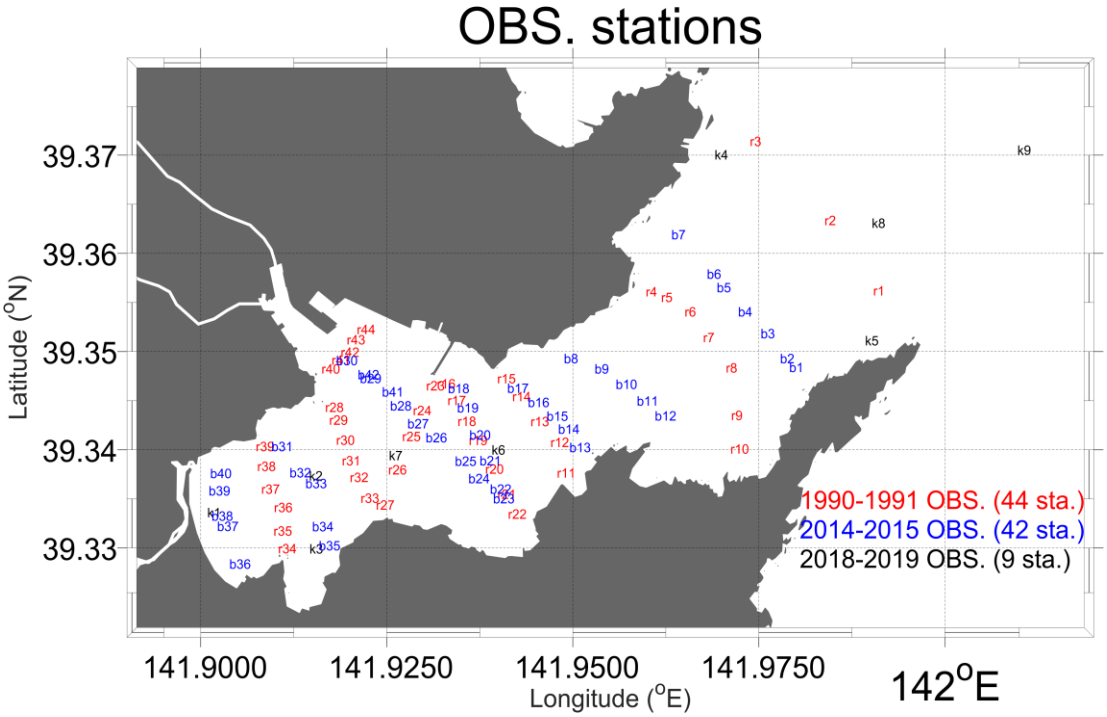

Fig.2.1-1, CTD observation stations. Red, blue, and black notations indicate 44 stations from 1990 to 1991, 42 stations from 2014 to 2015, and 9 stations from 2018 to 2019, respectively.

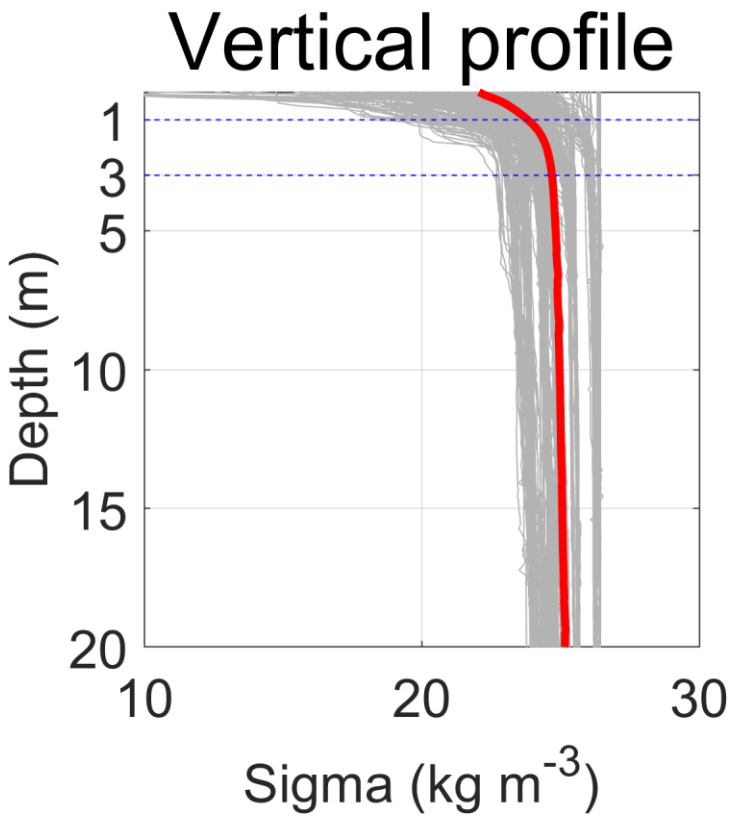

Fig.2.1-2, Vertical profile of density. Gray and red solid lines indicate the density profile of every observation in 2014s and the average of them, respectively. Blue dashed lines indicate the depth range where sea surface salinity was defined (1−3 m).

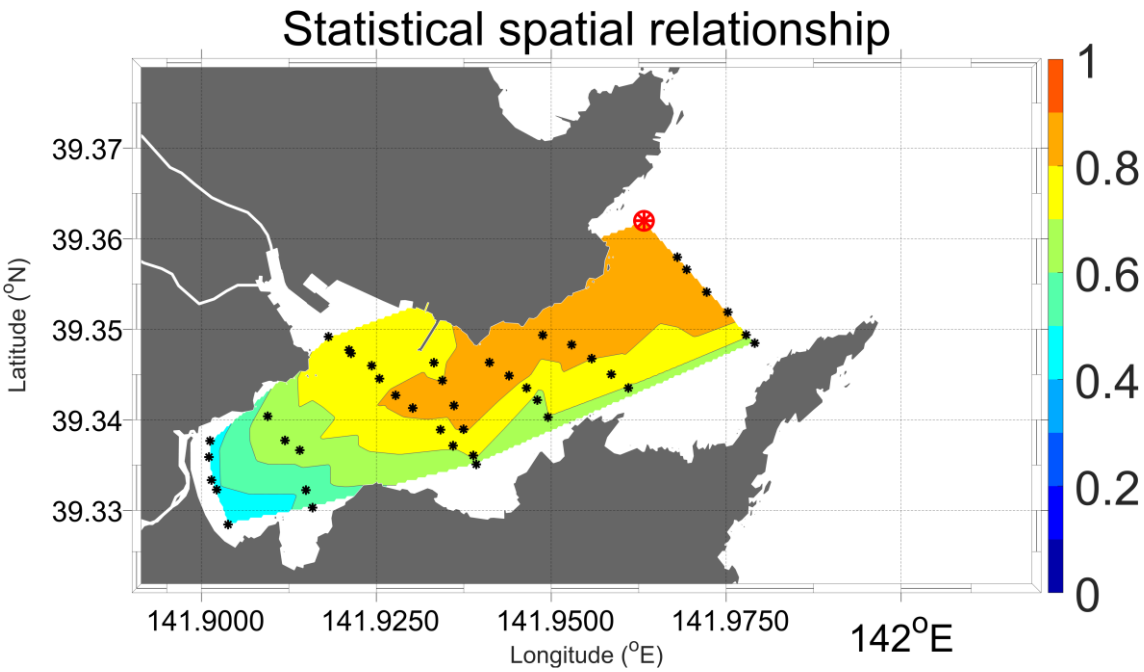

Fig.2.1-3, Correlation of observed sea surface salinity between big red point and other small black stations. Contours were made by linear interpolation.

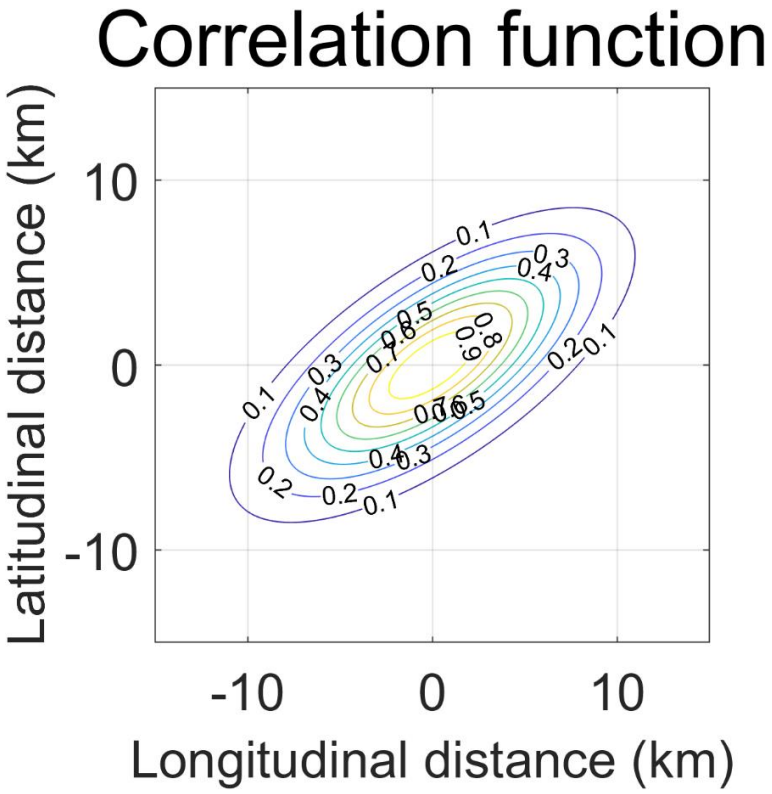

Fig.2.1-4, Spatial distribution of the formulated correlation function. Contour lines denoted correlation and they were anisotropic (ellipse-shaped).

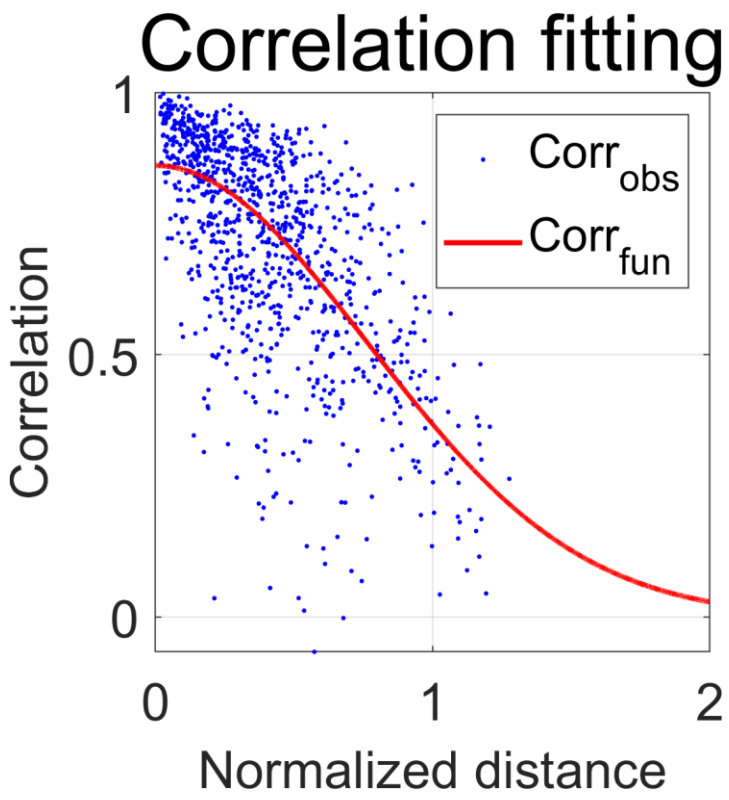

Fig.2.1-5, Curvature fitting (to equation 2.1.1) results to formulate the correlation function for the objective analysis. The normalization for distance was done as follows: With e-folding scale of correlation function (Fig.2.1-4) in all direction, the distance between observed stations were normalized by considering actual distribution of observed stations. Blue dots are correlations calculated between all pairs of observation stations. Red Gaussian bell curve is the correlation function that is obtained by curvature fitting from blue dots.

2.2 Numerical experiments

Numerical experiments were also performed to investigate the dynamics of circulation in the bay. We used CCSR Ocean Component Model version 4.0 (Hasumi, 2006), which is an ocean general circulation model with a z-coordinate system. The model is based on the hydrostatic and Boussinesq approximations with explicit free surface simulation. Smagorinsky viscosity (Smagorginsky, 1963) was used for the horizontal momentum mixing with adjustable parameter 2.8. Although it was twice of ordinarily (Rosati and Miyakoda, 1988), we used this value considering tidal mixing that was not reproduced here (Tanaka et al., 2008). Turbulence closure model of Noh and Kim (1999) was used for vertical eddy viscosity and diffusivity. Physical parameter of background vertical viscosity and diffusivity were 1×10^{-3} m^2 s^{-1}, and 3×10^{-5} m^2 s^{-1}, respectively (Rosati and Miyakoda, 1988; Tanaka et al., 2008).

The entire model domain is from 141.87 ºE to 142.17 ºE and 39.268 ºN to 39.475 ºN, and the region of main interest is in and around Otsuchi Bay (Fig. 2.2-1). Horizontal grid spacing is approximately 100 m both in longitudinal and latitudinal directions (258 × 230 grids). There were 41 levels in the vertical, with spacing of 2 m near the surface, smoothly increasing to about 15 m at the maximum depth of 260 m. The bottom topography was generated by side-scan sonar data (2 m resolution) for Otsuchi bay, and Japan Oceanographic Data Center data for other areas (Fig. 2.2-1). There are three rivers flowing into the bay: Otsuchi, Kozuchi, and Unosumai Rivers (Fig. 2.2-1). However, because Otsuchi and Kozuchi Rivers are unified at the estuary, we assumed them as a single river to summing up their volume transports in the model. Initial conditions were generated by temperature and salinity that were observed by Iwate Fisheries Technology Center (black dots in Fig.2.2-2): Monthly values observed outside the bay were averaged spatially over the model domain, and they were temporally interpolated to the time of the experiments. The initial conditions (Fig.2.2-3) were given uniform in horizontal. A closed boundary condition with lateral restoring layers was used. Outside the bay, values of the temperature and salinity are restored to the initial conditions during the experiments, the timescale of which was gradually distributed from 30 days to 12 hours (Fig.2.2-4).

There were many candidates for forcing that should play important roles in the circulation. In this study, we investigated the effects of river discharge (freshwater flux) and wind on the rotating frame. Monthly-averaged values were estimated for the forcings, using observational data that was obtained in and around Otsuchi Bay (Fig.2.2-2). We performed case study experiments by changing patterns of the forcings (Table.2.2-1).

In CCSR Ocean Component Model version 4.0, freshwater flux is given as sea surface flux (i.e., precipitation). Therefore, to generate the natural effect of river flow, we artificially made each river region with (200 m × 2100 m), where freshwater flux was imposed over the river surface (Fig. 2.2-1). The river discharge was estimated using the dataset that was produced by Adachi in 2013, who conducted observations of water levels continuously and flow velocities at intervals in Kozuchi river during a period from 2011 to 2013. On the basis of this directly-observed riverine data and nearby precipitation data (Shinmachi station, Japan Meteorological Agency; Blue-star at Fig. 2.2-2), we firstly estimated time series of daily river discharge for Otsuchi, Kozuchi, and Unosumai Rivers (Fig. 2.2-5), then estimated monthly river discharge by moving average with the window size of 30 days. Typical values of monthly averaged river discharge in the Otsuchi+Kozuchi and Unosumai were 0.56 $m^3 s^{-1}$ and 0.47 $m^3 s^{-1}$ in Case Win (winter), respectively and 2.96 $m^3 s^{-1}$ and 2.51 $m^3 s^{-1}$ in Case Sum (summer), respectively. Detailed algorisms for the estimation are given in the appendix (A.2.2-1).

The wind is also an important forcing in the ocean circulation. Stress of wind, which is imposed on the sea surface, was estimated on the basis of an anemometer in the bay (red triangle in Fig. 2.2-2) as follows. First, we converted the wind speed that was observed at a height of 7 m into that at a height of 10 m. According to Johnson (1999), the conversion relation is given by

$$\frac{U_{10}}{U_7} = \left(\frac{10}{7}\right)^{0.108}, \tag{2.2.1}$$

where U_{10} and U_7 were wind speed at height of 10 m and 7 m, respectively. Then, we converted the wind speed into the wind stress using a relationship (Cushman-Roisin and Beckers, 2008)

$$\tau = \rho_{air}\, C_d\, U_{10}\, |U_{10}|, \tag{2.2.2}$$

where ρ_{air} and C_d are 1.225 kg m^{-3} and 1.5×10^3, respectively. The estimated wind stresses in 2014 and 2015 are shown in Fig. 2.2-6. In addition, because of the lack of observed data in the bay, wind stress in 2014 was converted from the wind data at Kamaishi station (Japan Meteorological Agency; magenta-triangle at Fig. 2.2-2), using relationships between wind data of the Otsuchi Bay and Kamashi in 2015. Detailed converting processes are given in the appendix (A.2.2-2). The wind stress forcings were imposed mainly near the coastline, the values of which were gradually decreased to zero in the offshore area (Fig. 2.2-7). Typical values (direction) of the monthly averaged wind stresses were 0.024 N m^{-2} (northwesterly wind) and 0.006 N m^{-2} (southeasterly wind) in Case Win and Case Sum, respectively.

Table.2.2-1, Numerical experiment cases. Win / Sum (initial conditions) indicates initial conditions in Fig.2.2-1 (a) / (b), respectively. NW / SE (wind) indicate wind in Fig.2.2-7 (a) / (b), respectively. H / L (river) indicate 2.96 $m^3 s^{-1}$ and 2.51 $m^3 s^{-1}$ / 0.56 $m^3 s^{-1}$ and 0.47 $m^3 s^{-1}$ for Otsuchi+Kozuchi and Unosumai Rivers, respectively.

	Initial conditions	Wind	River
Case Win R	Win	-	L
Case Sum R	Sum	-	H
Case Win RW	Win	NW	L
Case Sum RW	Sum	SE	H

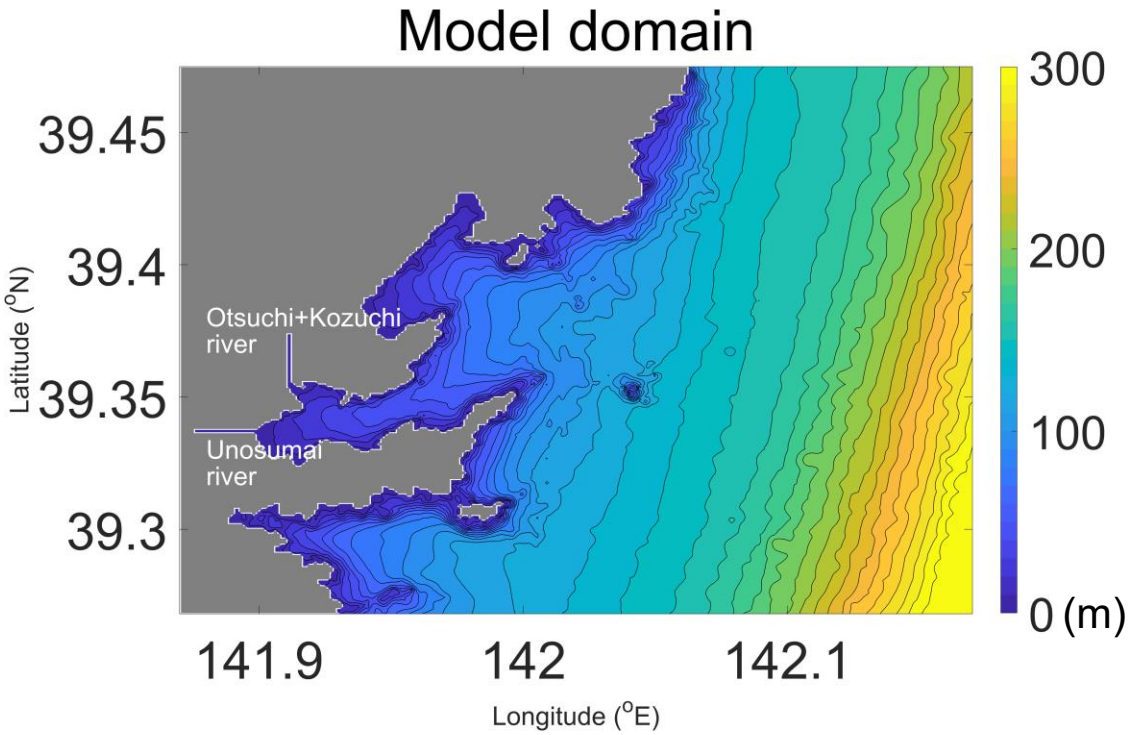

Fig.2.2-1, The domain of numerical experiments. The gray area denotes the land, and colored contour indicated the bottom topography.

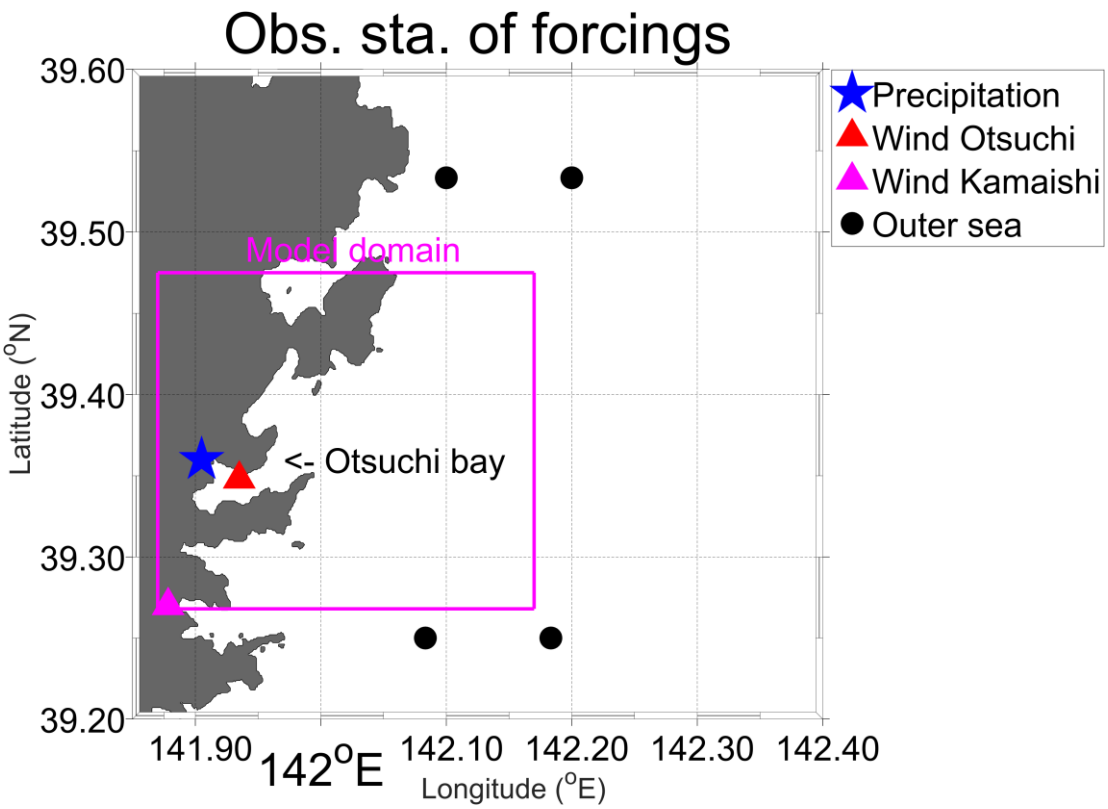

Fig.2.2-2, Observation stations for the forcing data that were used in numerical experiments. The pink rectangle shows the domain of the numerical experiment. The initial conditions were based on the monthly CTD observation data (black points; Iwate Fisheries Technology Center). The wind stress was derived from anemometer observation data in Otsuchi Bay (red triangle; The University of Tokyo; 7 m in height, 10 minutes interval wind data), and in Kamaishi station (magenta triangle; Japan Meteorological Agency; 1 hour interval wind data). River discharge data was estimated from the precipitation data in Shinmachi station (blue star; Japan Meteorological Agency; daily precipitation data).

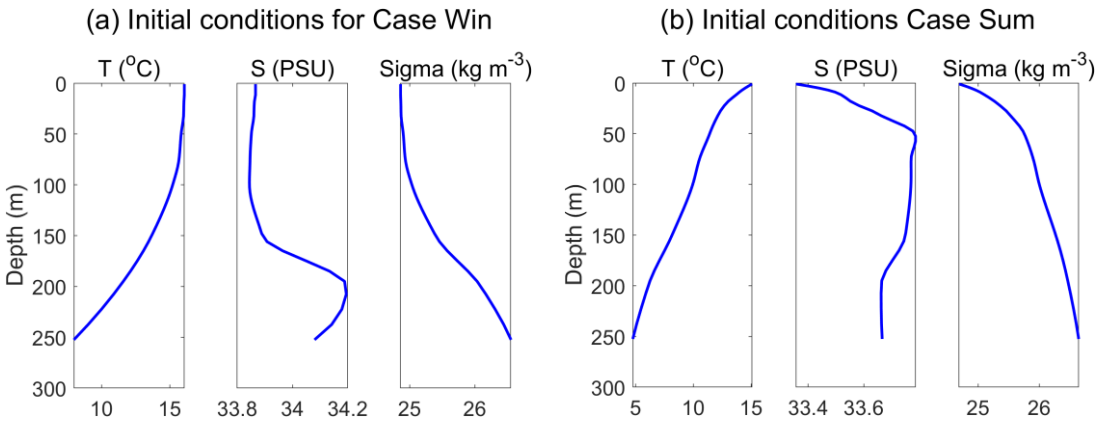

Fig.2.2-3, Initial conditions of numerical experiments. Blue line indicated initial conditions (temperature, salinity, and density). The left panel (a) shows initial conditions for the Case Win, and the right panel (b) shows for the Case Sum.

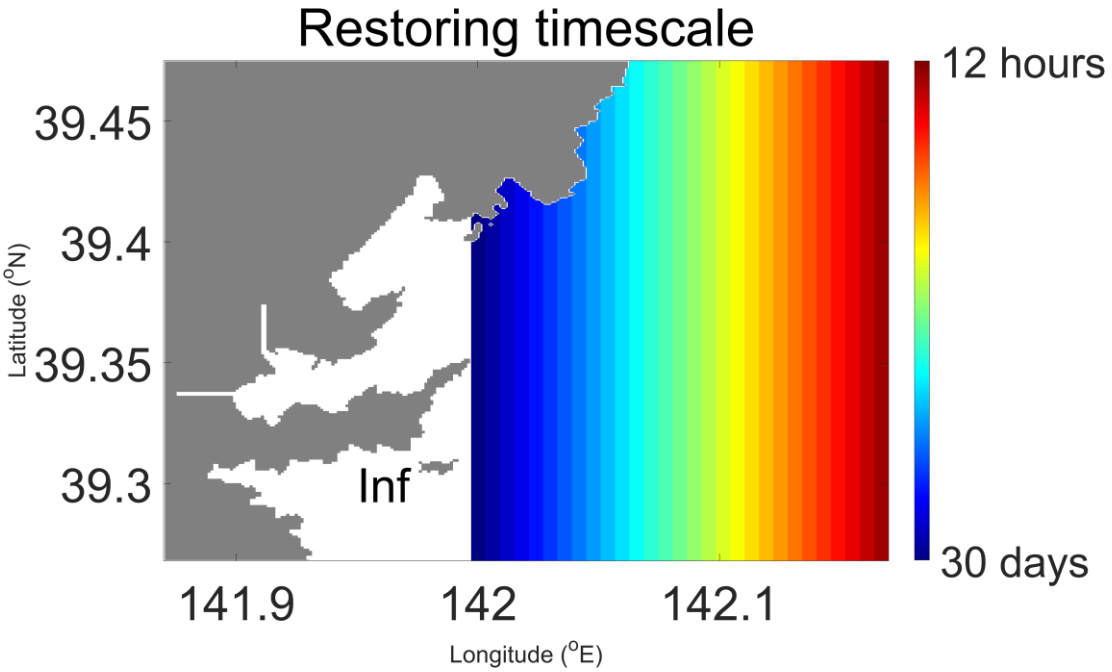

Fig.2.2-4, Restoring timescale. Colored contour indicates restoring timescale which gradually varies from 30 days to 12 hours.

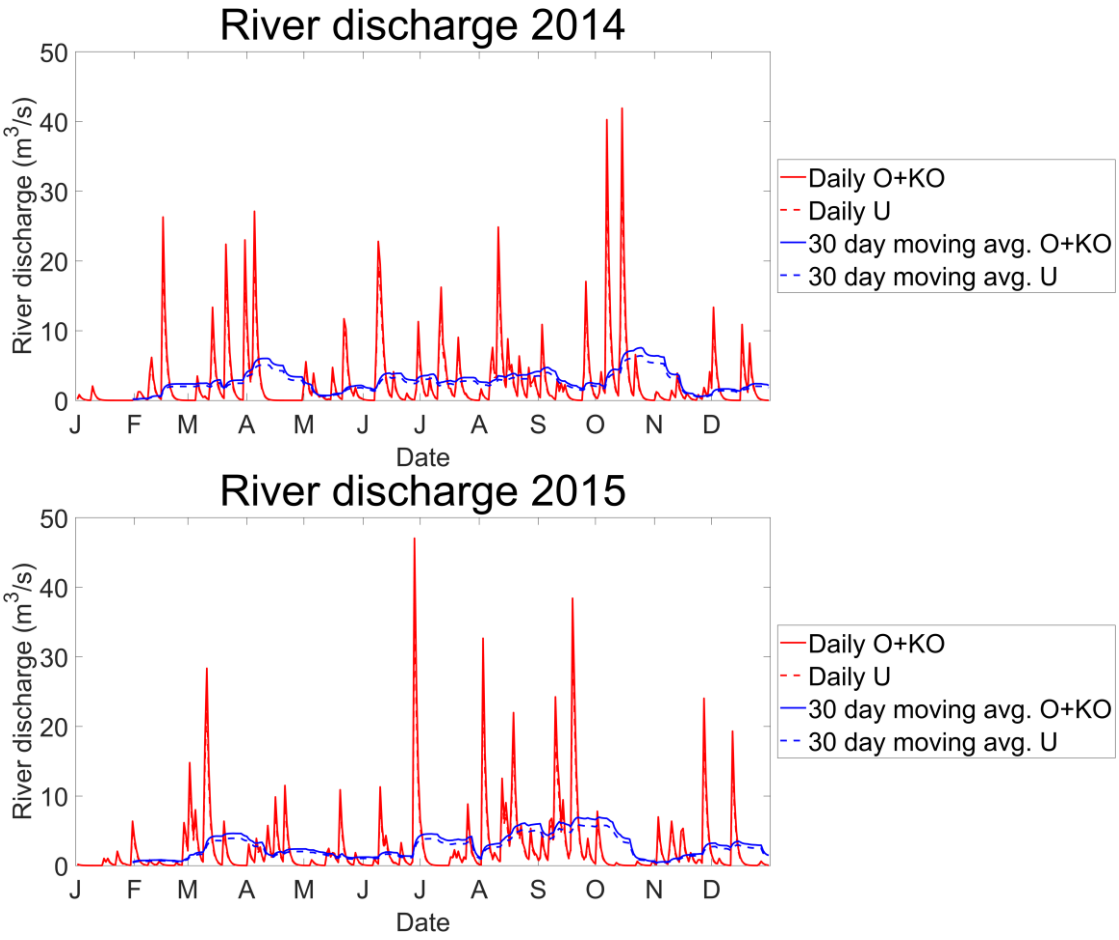

Fig.2.2-5, Estimated time series of river discharge in 2014 and 2015. The red solid lines indicate the daily variation of Otsuchi+Kozuchi Rivers (O+KO), and the red dotted lines indicate the daily variation of Unosumai River (U). The blue solid lines indicate 30 days moving average of the Otsuchi+Kozuchi Rivers, and the blue dotted lines indicate 30 days moving average of the Unosumai River.

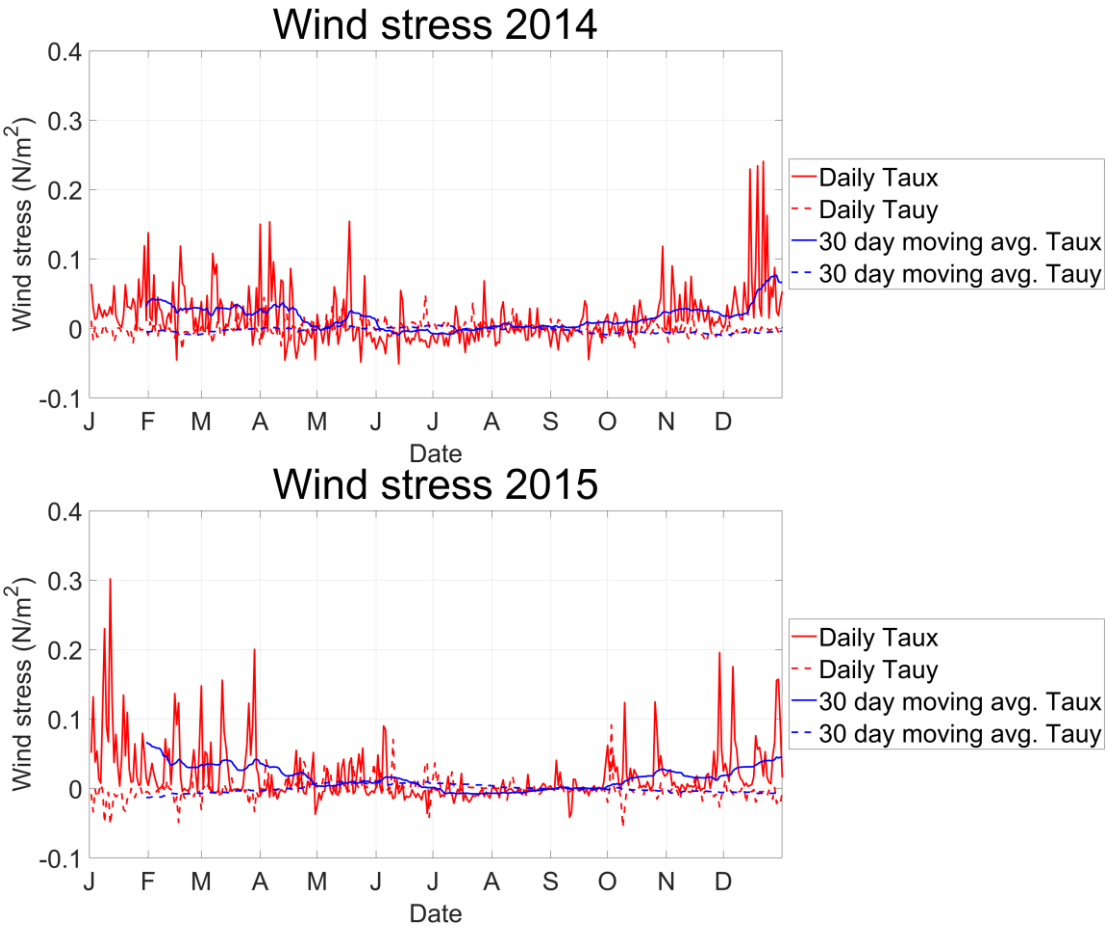

Fig.2.2-6, Estimated time series of wind stress in 2014 and 2015. The red solid lines indicate daily zonal wind stress and the red dotted lines indicate daily meridional wind stress. The blue solid lines indicate 30 days moving average of zonal wind stress and the blue dotted lines indicate 30 days moving average of meridional wind stress. The upper panel, was estimated by the observed wind in Kamaishi (magenta triangle in Fig.2.2-2) and the below panel, was estimated by the observed wind in Otsuchi Bay (red triangle in Fig.2.2-2), because there was no observed wind data in Otsuchi Bay in 2014.

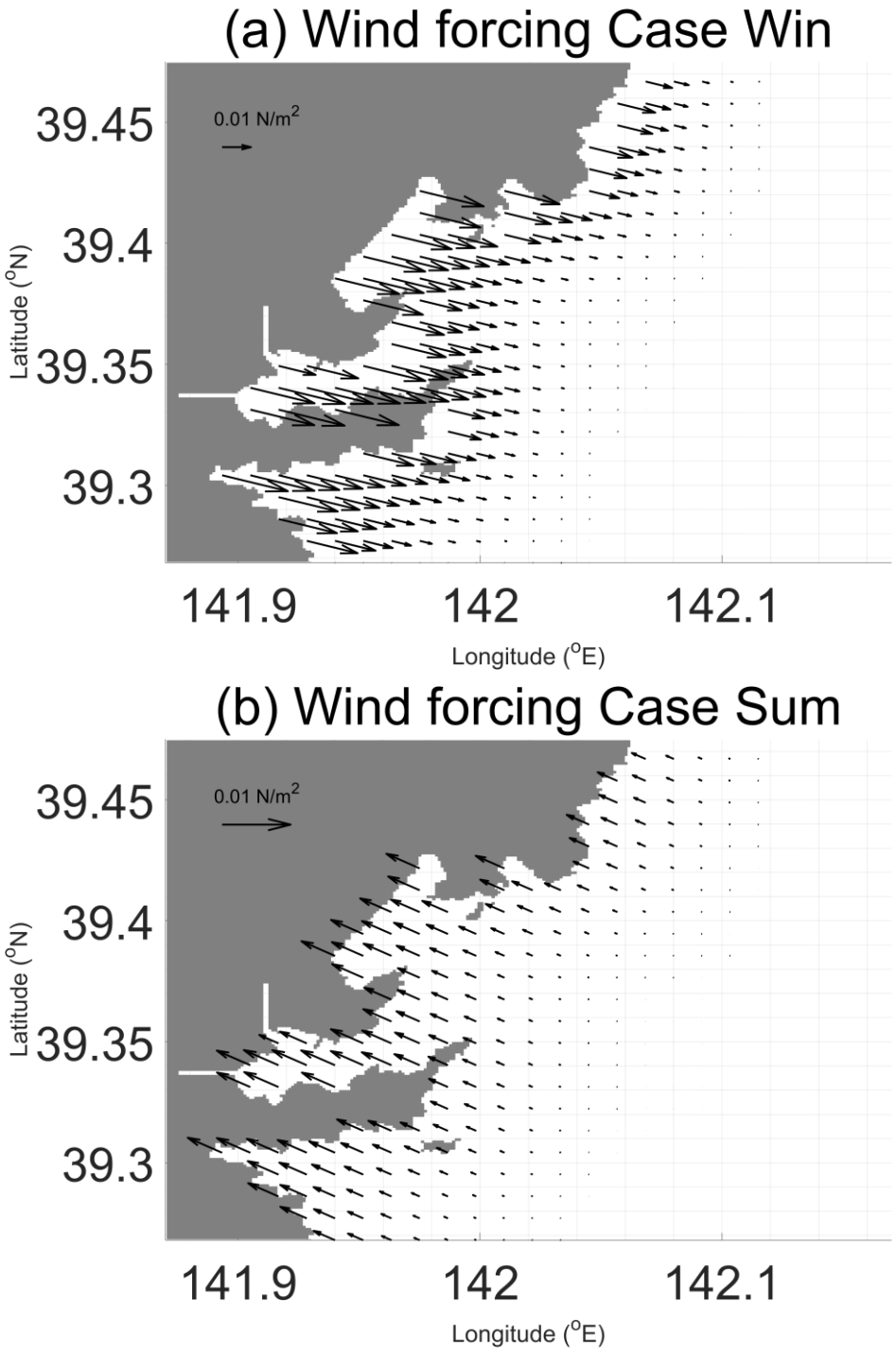

Fig.2.2-7, Wind forcing in (a) Case Win RW and (b) Case Sum RW.

3. Results and Discussion

3.1 Observational data analysis

First, we take a look at the objective analysis results of the sea surface salinity. There were two patterns of circulation in Otsuchi Bay. In the first pattern, high-salinity water existed near the northern coast, whereas low-salinity water existed near the southern coast. In the second pattern, low-salinity water existed near the northern coast, whereas high-salinity water existed near the southern coast. Both patterns formed steep salinity gradients in meridional (i.e., cross-bay) directions. In this study, the first pattern is referred to as a positive salinity gradient pattern, whereas the second pattern is referred to as a negative salinity gradient pattern. As an example of the positive salinity gradient pattern, the objective analysis result for November 6th, 2015 is shown in Fig. 3.1-1. In contrast, as an example of the negative salinity gradient pattern, the objective analysis result for June 26th, 2014 is shown in Fig. 3.1-2. According to the previous theories (e.g. Minato, 1983), river water tends to flow with the coast to the right in the northern hemisphere, when the Earth's rotation affects the motion of the river water. Therefore, it was suggested that low-salinity water might only exist near the southern coast and always form positive salinity gradient patterns. However, it is interesting that the negative salinity gradient pattern was also found in the real sea.

To compare all the observational patterns quantitatively, we defined the salinity gradient as the spatially averaged one over the region indicated by Fig.3.1-3 with the equation

$$Salinity\ gradient = \frac{\overline{\Delta S}}{\Delta\, distance} = \frac{\overline{S(x_1,x_2)}}{dist(x_1,x_2)}\ , \qquad (3.1.1)$$

where, x_1 and x_2 are locations,

x_1: $(141.9619^{o}\mathrm{E}, 39.3537^{o}\mathrm{N}), (141.9599^{o}\mathrm{E}, 39.3531^{o}\mathrm{N}), \dots, (141.9443^{o}\mathrm{E}, 39.3483^{o}\mathrm{N})$

x_2: $(141.9665^{o}\mathrm{E}, 39.3447^{o}\mathrm{N}), (141.9645^{o}\mathrm{E}, 39.3441^{o}\mathrm{N}), \dots, (141.9488^{o}\mathrm{E}, 39.3394^{o}\mathrm{N})$.

The locations x_1 and x_2 were near the northern coastline and southern coastline of the bay, respectively. As a result, positive salinity gradient patterns were dominant, while negative gradient patterns sometimes occurred in summer or early fall (Fig.3.1-4). There was no distinguished difference between 2014s and 1990s.

Moreover, we estimated the internal Rossby deformation radii in the area where the river water accumulated within the defined region of the salinity gradient (among Stas. 8 to 17 in 2014s and Stas. 4 to 15 in 1990s). According to Gill (1982), the internal Rossby deformation radius in a two-layers system is given

$$R_d = \left[(\Delta\rho g/\rho)\, h_{up} h_{down}/\left(h_{up} + h_{down}\right)\right]^{\frac{1}{2}}/f\,, \qquad (3.1.2)$$

where, f (= 9.25×10^{-5} s^{-1}) is the Coriolis parameter, g (= 9.81 m s^{-2}) is the gravitational acceleration, ρ is average density of water, $\Delta\rho$ is density difference between upper and lower layers, and h_{up} and h_{down} are thickness of the upper and lower layers, respectively. The thickness of the upper layer was set to be 3 m on the basis of the observation result (Fig.2.1-2), and the density difference between the upper and lower layers was calculated after averaging water density in each layer.

As mentioned above, the theoretical studies suggested that river water tends to flow with the coast to the right under the effect of the Earth's rotation (e.g., Minato, 1983). The internal Rossby deformation radius is the length scale of geostrophic adjustment due to the Earth's rotation. Therefore, the river water is generally confined within the internal Rossby deformation radius from the coast. Thus, the positive salinity gradient pattern on November 6th, 2015 (indicated by a circle in Fig.3.1-4) may be explained by the small deformation radius on that day (indicated by a circle in Fig.3.1-5). In contrast, the negative salinity gradient pattern on June 26th, 2014 (indicated by a triangle in Fig.3.1-4) may be explained by the large deformation radius on that day (indicated by a triangle in Fig.3.1-5). Considering these observational results, we present a hypothesis that the relationship between the salinity gradients and the internal Rossby deformation radii would be as follows: If there is no river discharge and homogenous, there must be zero salinity gradient, as well as, the zero internal Rossby deformation radius. As river discharge increase from zero, it would form or strengthen the stratification. Therefore, the internal deformation radius would also increase. Consequently, the salinity gradient would increase. However, as the internal Rossby deformation radius becomes nearly, or exceeds a certain threshold, i.e., half of the width of the bay (1000 m), the salinity gradient would start to decrease by the spilled river water. Indeed, these relationships may be seen in Fig.3.1-5: The large positive values of the salinity gradient were observed in the medium range of the internal Rossby deformation radius between 1000 m and 2000 m. Moreover, large negative values of the salinity gradient were observed when the internal Rossby deformation radius was larger than 2000 m, which is the width of the bay. However, it should be noted that a large variance existed in the relation between the deformation radius and the salinity gradient, as seen in Fig.3.1-5. This large variance implies that the salinity distribution may be determined not only by the river discharge and the Earth's rotation effect, but also by another factor (forcing), which is investigated in the following sections.

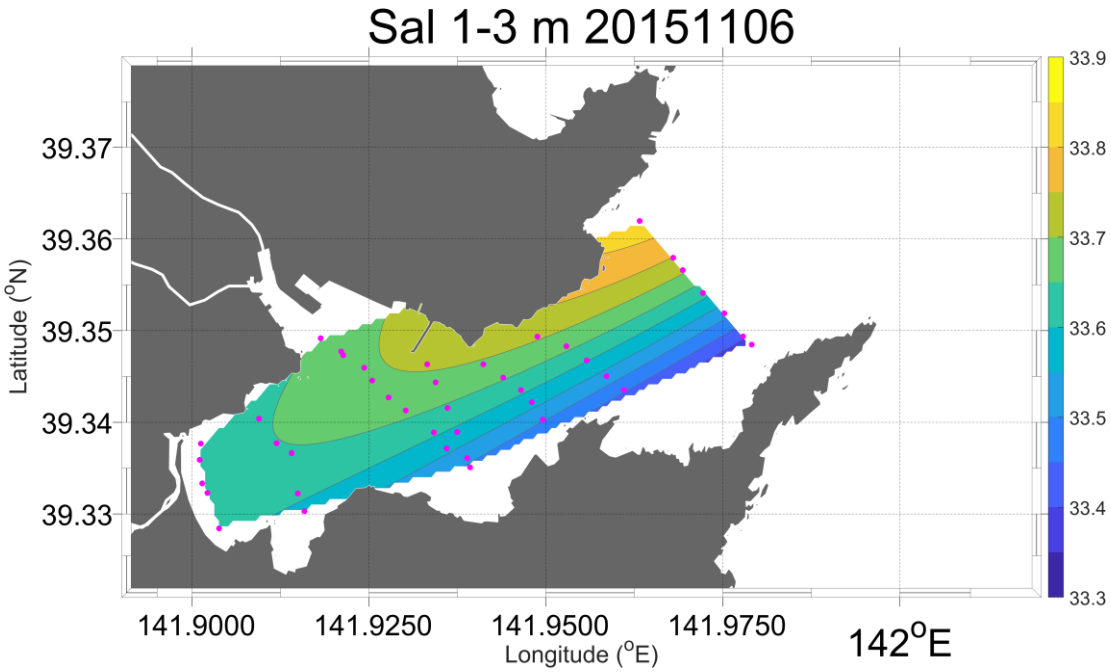

Fig.3.1-1, Representative positive salinity gradient pattern of sea surface salinity map on November 6th, 2015, which was produced by the objective analysis. The pink dots indicate CTD observation stations.

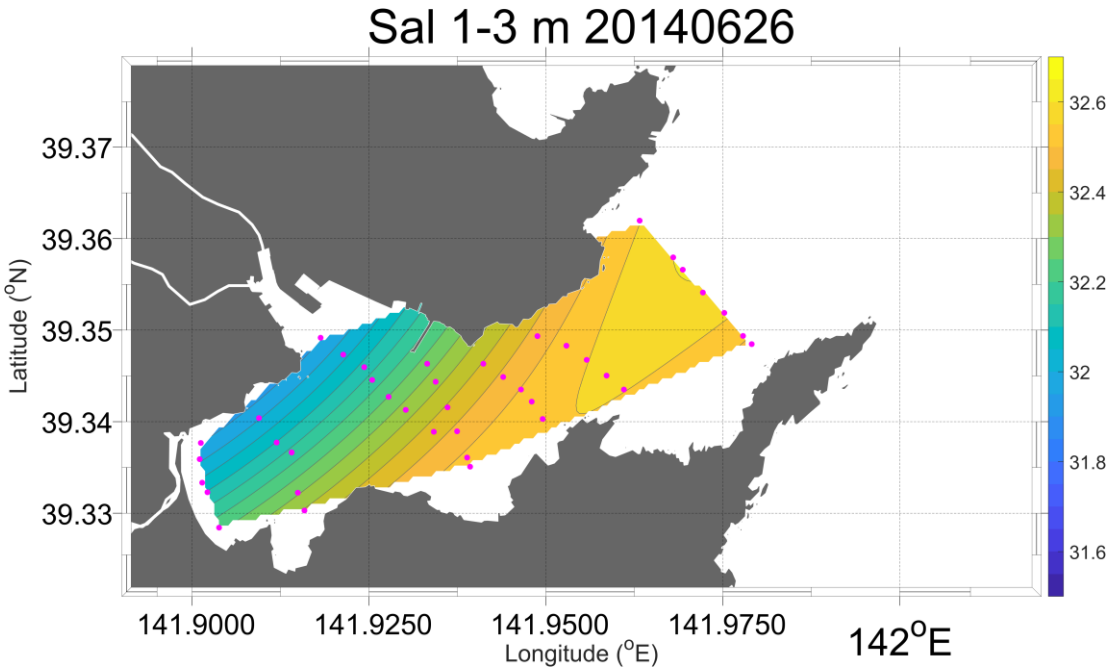

Fig.3.1-2, Representative negative salinity gradient pattern of sea surface salinity map on June 26th, 2014, as in Fig.3.1-1, but with different color index.

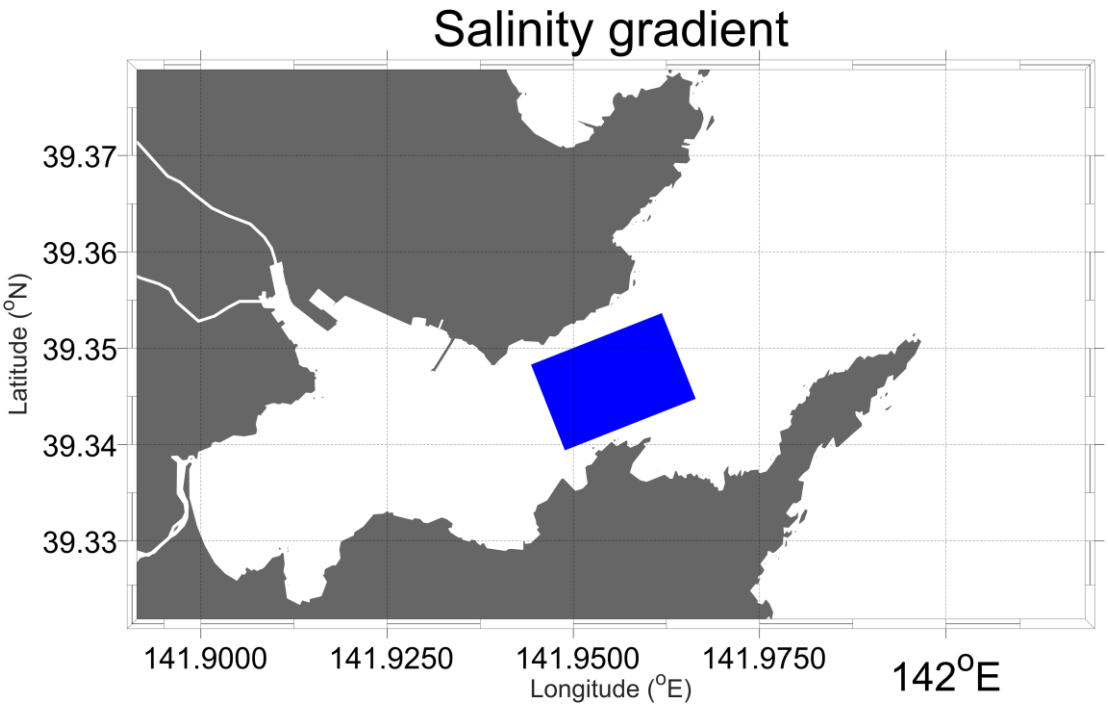

Fig.3.1-3, Region where the salinity gradients were calculated. The salinity gradients were averaged over this region.

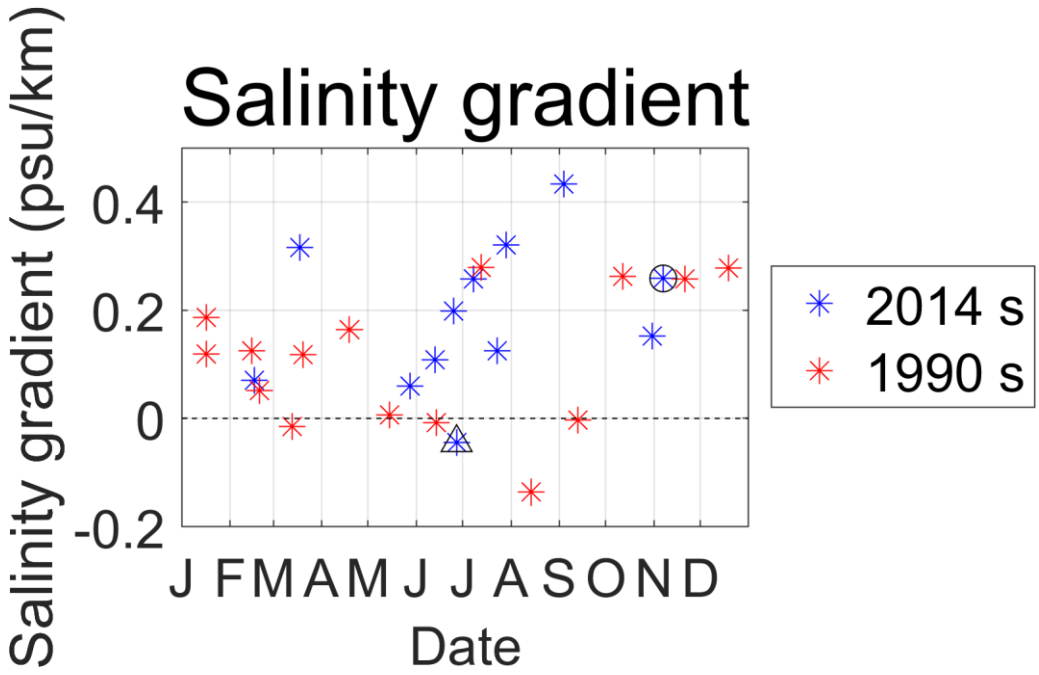

Fig.3.1-4, Salinity gradient variation. Blue dots indicate the salinity gradient from 2014 to 2015 and red dots indicate salinity gradient from 1990 to 1991. The blue dot with a black circle indicates the positive salinity gradient pattern on November, 6th, 2015 and the blue dot with a black triangle indicates the negative salinity gradient on June, 26th, 2014.

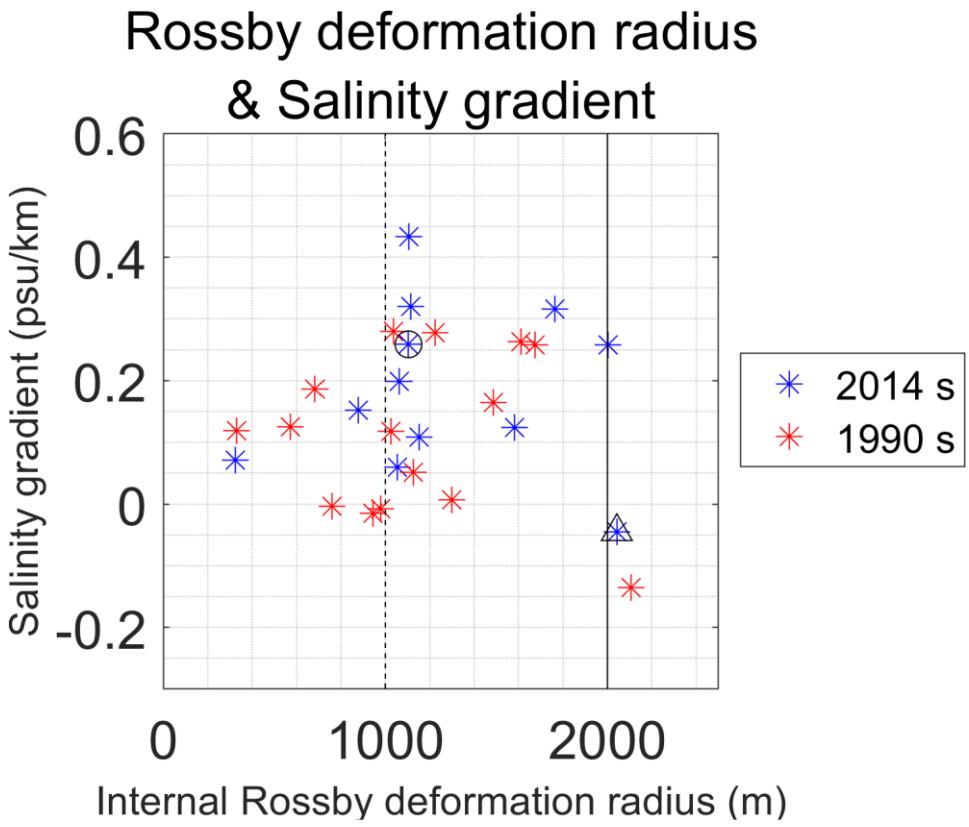

Fig.3.1-5, The Internal Rossby deformation radii and the salinity gradients. The blue dots indicate the values from 2014 to 2015 and the red dots indicate the values from 1990 to 1991. Black solid and dashed line indicate width and its half of the bay, respectively. The blue dot with a black circle indicates the positive salinity gradient pattern and internal Rossby deformation radius on November, 6th, 2015 and the blue dot with a black triangle indicates the negative salinity gradient and internal Rossby deformation radius on June, 26th, 2014.

3.2 Theory of river water spread

In section 3.1, we suggested the hypothesis of the increasing and decreasing relationship between the salinity gradients and the internal Rossby deformation radii. In this section, we considered a simple theory for river water spread in Otsuchi Bay which may be related to our hypothesis.

The geometry of river water flow can be simplified as shown in Fig.3.2-1, where h_p, h_u, h_d, ρ_p, and ρ_{amb} denote the total thickness of the river water flow, upper triangle (blue) thickness, lower triangle (yellow) thickness, the average density of river water flow, and background density, respectively. Based on the observation, we assumed that the total thickness of river water flow is 3 m (Fig.2.1-2). The width of river water flow could be expressed as a summation of internal Rossby deformation radius and distance from the coast which is related to the slope of the bottom topography (Lentz and Helfrich, 2002). However, we neglected the distance from the coast ($\cong 30$ m), because it was small enough compared to the observed the internal Rossby deformation radii. In other words, we assumed that the width of the river water flow only depends on the internal Rossby deformation radius (R_d). Lentz and Helfrich (2002) suggested that the internal Rossby deformation radius is related to river discharge (Q) that

$$R_d \approx \frac{(2Qg'f)^{\frac{1}{4}}}{f} \tag{3.2.1}$$

where Q, f, and g' are river discharge, Coriolis parameter, and reduced gravity. If we assumed that there is no mixing between discharged river water and ambient water in the bay in this step, the discharged river water would form the blue triangle in Fig.3.2-1, because river water density (ρ_f) is lighter than ambient water density (ρ_{amb}) in the bay. Therefore, the thickness of the upper blue triangle (h_u) would be a function of river discharge (Q) that

$$Q = \frac{h_u R_d}{2} U\,. \tag{3.2.2}$$

The velocity (U) can be obtained from the geostrophic balance

$$fU = \frac{1}{\rho}\frac{\partial p}{\partial x} \tag{3.2.3}$$

where $\frac{\partial p}{\partial x}$ is pressure change over distance from the coast. Under the hydrostatic approximation, equation (3.2.3) can be rewritten that

$$U = \frac{1}{\rho_{amb}}\frac{\rho_f g h_u}{R_d f}. \tag{3.2.4}$$

Since we assumed no mixing between discharged river water and ambient water in the bay, the reduced gravity is

$$g' = \frac{\rho_{amb} - \rho_f}{\rho_{amb}} g, \tag{3.2.5}$$

where ρ_{amb} is assumed as the density of depth (3 m to bottom) and time-averaged salinity (33.7 psu; S_{amb}) and temperature (12.6 ºC) of whole observation data, and ρ_f is assumed as the density of zero salinity (0 psu) and the same temperature (12.6 ºC). The density (ρ) can be estimated by the linear equation of state which is

$$\rho = \rho_o + \alpha(T - T_o) + \beta(S - S_o) \tag{3.2.6}$$

where, ρ_o, α, T_o, β, and S_o are 1027 kg m^{-3}, -0.15 kg m^{-3} ºC^{-1}, 10 ºC, 0.78 kg m^{-3} psu^{-1}, and 35 psu, respectively (Knauss, 1997). The typical value of ρ_{amb} and ρ_f are 1026 and 999 kg m^{-3}, respectively. With equations 3.2.1 to 3.2.5 and total thickness of river water flow (3 m), we can estimate the depth of lower triangle (yellow) thickness (h_d) that

$$h_d = 3 - h_u. \tag{3.2.7}$$

As a next step, we considered the density of the river water flow (ρ_p). In this step, we assumed that the two triangles in Fig.3.2-1 are well-mixed. Since the mass should be conserved, the density of the river water flow (ρ_p) is

$$\rho_p = \frac{\rho_{amb}(h_d R_d L/2) + \rho_f(h_u R_d L/2)}{total\ thickness \times R_d L/2} = \frac{\rho_{amb} h_d + \rho_f h_u}{3} \tag{3.2.8}$$

where, $hR_dL/2$ is the volume of the triangular prism with density ρ. With obtained river water flow density (ρ_p), we could estimate its salinity (S_p) by equation 3.2.6 that

$$S_p = \frac{\rho_p - \rho_o - \alpha(T - T_o)}{\beta} + S_o = \frac{\rho_p - 1026.6}{0.78} + 35. \tag{3.2.9}$$

As we assumed that salinity in river water flow is well mixed, we could reconstruct the preliminary sea surface salinity as shown in schematics in Fig.3.2-2 (black solid line). It should be noted that we did not consider lateral mixing, therefore, the preliminary reconstructed salinity is discontinuous. In order to calculate the salinity gradient, we first estimated the mean sea surface salinity ($\bar{S}$) which is shown red dotted line in Fig.3.2-2. Considering that the width of the bay (W) is 2000 m, the mean salinity ($\bar{S}$) would be

$$\bar{S} = \frac{S_p R_d + S_{amb}(W - R_d)}{W} = \frac{S_p R_d + 33.7(2000 - R_d)}{2000}\ . \tag{3.2.10}$$

Assume that sea surface salinity is linearly variated by distance, the reconstructed salinity (solid red in Fig.3.2-2) would meet the mean salinity in the middle of the bay, because it should have the same mean value. Therefore, the salinity gradient would be

$$Salinity\ gradient\ (psu/km) = \begin{cases} \frac{S_{amb}-\bar{S}}{1\ km} & \left(\bar{S} > \frac{S_{amb}+S_p}{2}\right) \\ \frac{S_{amb}-S_p}{2\ km} & \left(\bar{S} = \frac{S_{amb}+S_p}{2}\right) \\ \frac{\bar{S}-S_p}{1\ km} & \left(\bar{S} < \frac{S_{amb}+S_p}{2}\right) \end{cases} . \quad (3.2.11)$$

With this simple theory, we estimated the relationship between the salinity gradient and internal Rossby deformation radius by varying the river discharge (Q). It should be noted that our estimation applied until the internal Rossby deformation radius reached the width of the bay (2000 m).

Fig.3.2-3 shows the theoretical estimation of the relationship between the internal Rossby deformation radius and salinity gradient. As we hypothesize in section 3.1, the salinity gradient has a nonlinear relationship with the river discharge. The salinity gradient increases with increasing river discharge when the internal Rossby deformation radius is smaller than half of the width of the bay. On the other hand, the salinity gradient decreases with increasing river discharge when the radius is larger than half of the width of the bay. Therefore, the increasing and decreasing salinity gradient with respect to the internal Rossby deformation radii in the observation may be explained by this theory. However, since we assumed consistent ambient density and neglected the wind-induced circulations, the large variance in observation cannot be explained by this theory. The last thing that should be noted here is that the river discharge and internal Rossby deformation radius also have a nonlinear relationship, which implies the complexity of the river water spread in the bay.

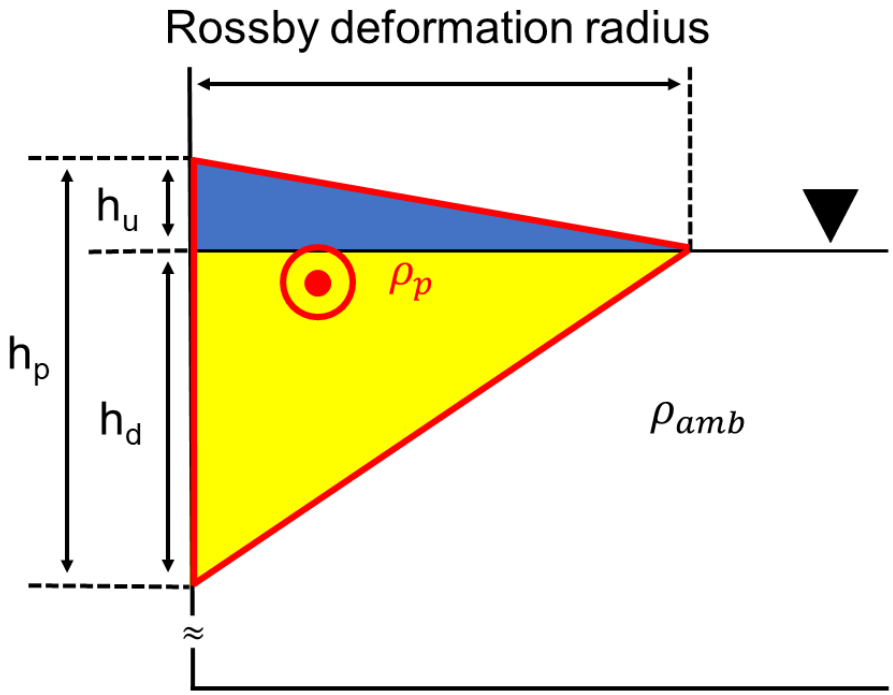

Fig.3.2-1, Schematic figure of geometry of river water flow.

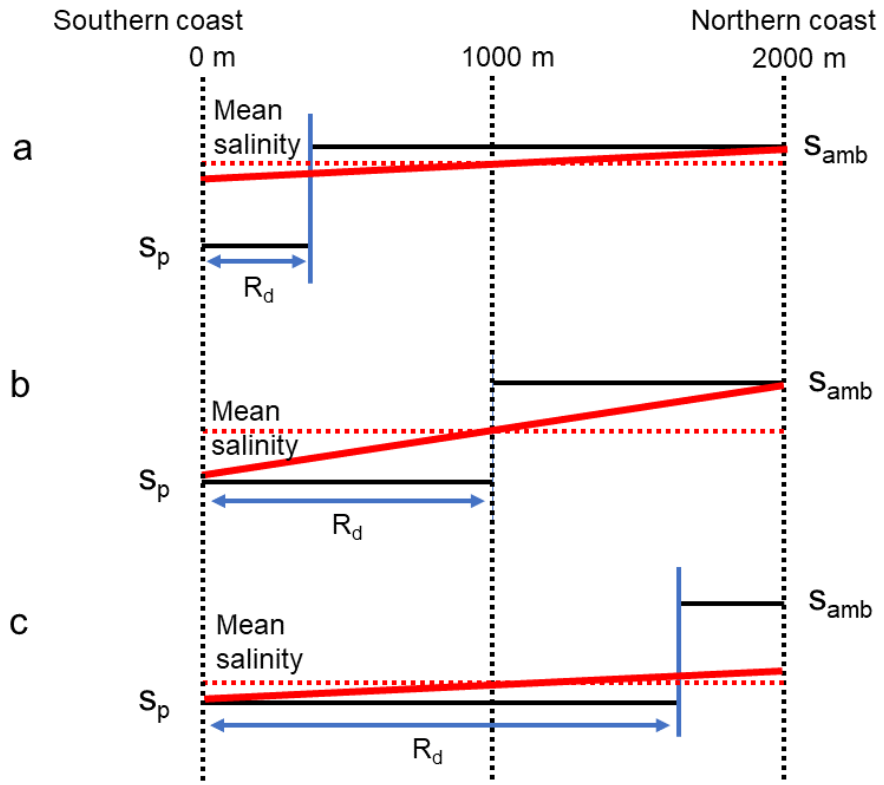

Fig.3.2-2, Schematic figure of salinity gradient estimation. (a), (b), and (c) indicate when mean salinity ($\bar{S}$) is larger, equal, and smaller compared to (S_{amb}+S_p) / 2.

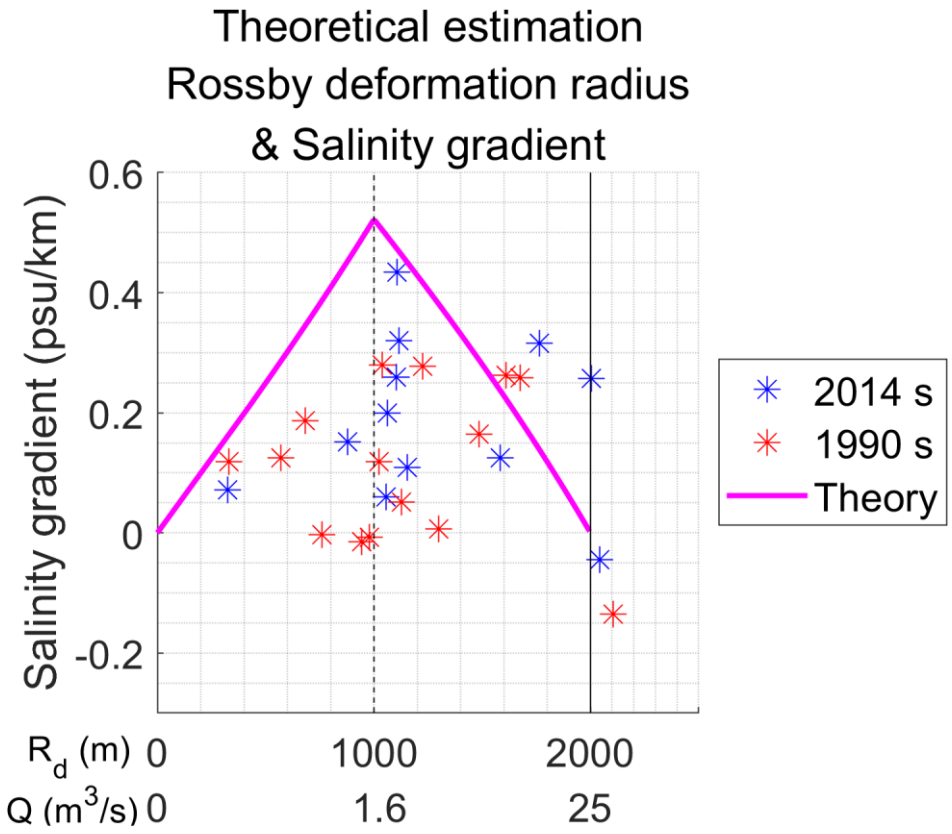

Fig.3.2-3, Theoretical estimation of salinity gradient and internal Rossby deformation radius. Blue points and red points are same as Fig.3.1-5, but with the theoretical estimation (magenta solid line).

3.3 Representative results in the numerical experiments

In section 3.1, it was suggested that the salinity gradients may be explained by the ratio of the bay width to the internal Rossby deformation radius, and the theory in section 3.2 may support our hypothesis. However, there was a large variance in the suggested relations (Fig.3.1-5). Therefore, to investigate in detail physical processes of the circulation in the bay, we performed numerical experiments for the two representative observed results (Table.2.2-1): November 6th, 2015 (positive salinity gradient pattern), and June 26th, 2014 (negative salinity gradient pattern).

First, we performed two experiments where only the river discharge was imposed as external forcing, which are referred to as Case Win R (for November 6th, 2015) and Case Sum R (for June 26th, 2014). The results of Cases Win R and Sum R are shown in Fig.3.3-1. With the same methods of estimating salinity gradient and internal Rossby deformation radius in section 3.1, the salinity gradient in Case Sum R was -0.08 psu km^{-1} and the internal Rossby deformation radius was 1.2 times larger than the width of the bay. Therefore, this result supports the hypothesis that the negative salinity gradient pattern could be generated with the larger internal Rossby deformation radius compared to the width of the bay. However, it should be noted that there is a large quantitative difference between the experiment and observation. Moreover, Case Win R did not reproduce the observed positive salinity gradient pattern not only qualitatively, but also quantitatively.

Then, we performed two further experiments where both the river discharge and the wind stress were imposed as external forcing, which are referred to as Cases Win RW and Sum RW. The results of Cases Win RW and Sum RW are shown in Fig.3.3-2. The former (Case Win RW) included the northwesterly wind (Fig.2.2-7 a), and it successfully reproduced the positive salinity gradient pattern qualitatively (Fig.3.3-2 a). To investigate the effect of the northwesterly wind on the circulation below the sea surface, Figures 3.3-3 and 3.3-4 show vertical sections of zonal velocities and salt flux, respectively, for the winter cases. Estuary circulation and associated salt flux from the Pacific were reinforced by the northwesterly wind, as suggested in previous studies from the observational data (Otobe et al., 2009; Ishizu et al. 2017). Moreover, the upwelling and downwelling were strengthened on the northern and southern coasts, respectively by the wind (Fig.3.3-5). The northwesterly wind-induced Ekman flow to transport surface riverine water southward, while subsurface high salinity water upwelled along the northern coast. Thus, the wind-induced upwelling of the high-salinity water along the northern coast played an important role in the formation of the positive salinity gradient pattern. It also should be noted that the wind-induced upwelling is also expected to provide nutrients from the subsurface to the surface. As suggested in the previous studies (Furuya et al. 1993; Kawamiya

et al. 1996; Kishi et al. 2003), upwelled nutrients would result in plankton blooming and the productivity of the aquaculture in the bay. Therefore, these results suggest that the northwesterly wind plays important roles in the circulation in the bay.

In contrast, the latter experiment (Case Sum RW), which included the southeasterly wind (Fig.2.2-7 b), did not improve the difference in the negative salinity gradient pattern between the experiment and the observation (Fig.3.3-2 b). Actually, the southeasterly wind slightly increased the difference between the observational result and the numerical experiment. This may be related to the phenomena that the southeasterly wind weakened the estuary circulation slightly (Fig.3.3-6), and it changed the distribution of up/downwelling areas slightly (Fig.3.3-7). That is southeasterly winds may not be important compared to northwesterly winds, and the asymmetric effects of the winds on the circulation might be a cause of the large variance in the relation between the internal deformation radius and the salinity gradient, the details of which should be investigated in the future.

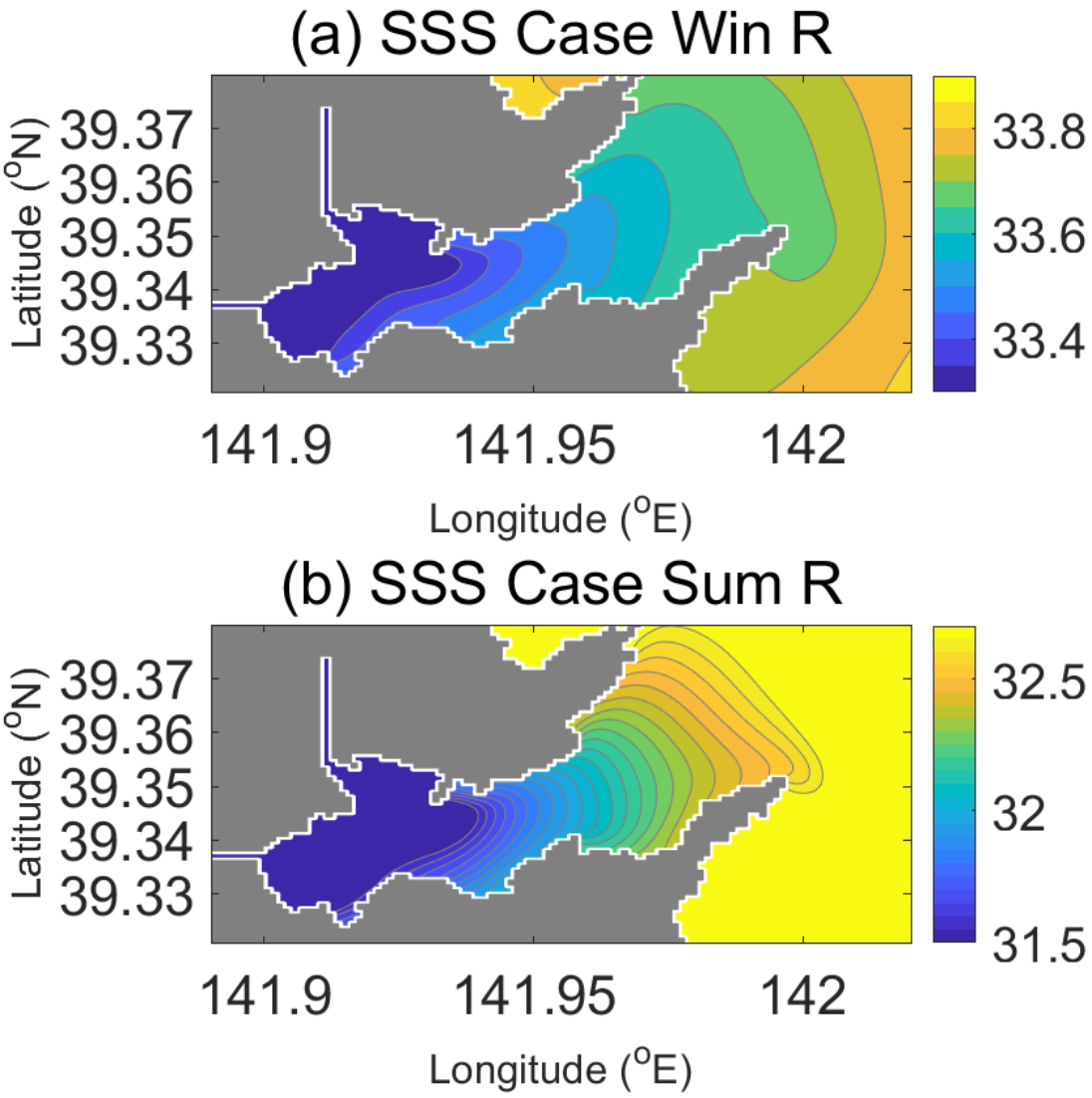

Fig.3.3-1, Sea surface salinity in (a) Case Win R and (b) Case Sum R on the 30th day of numerical experiments. Colored contour indicates the salinity. It should be noted that color index is different between (a) and (b).

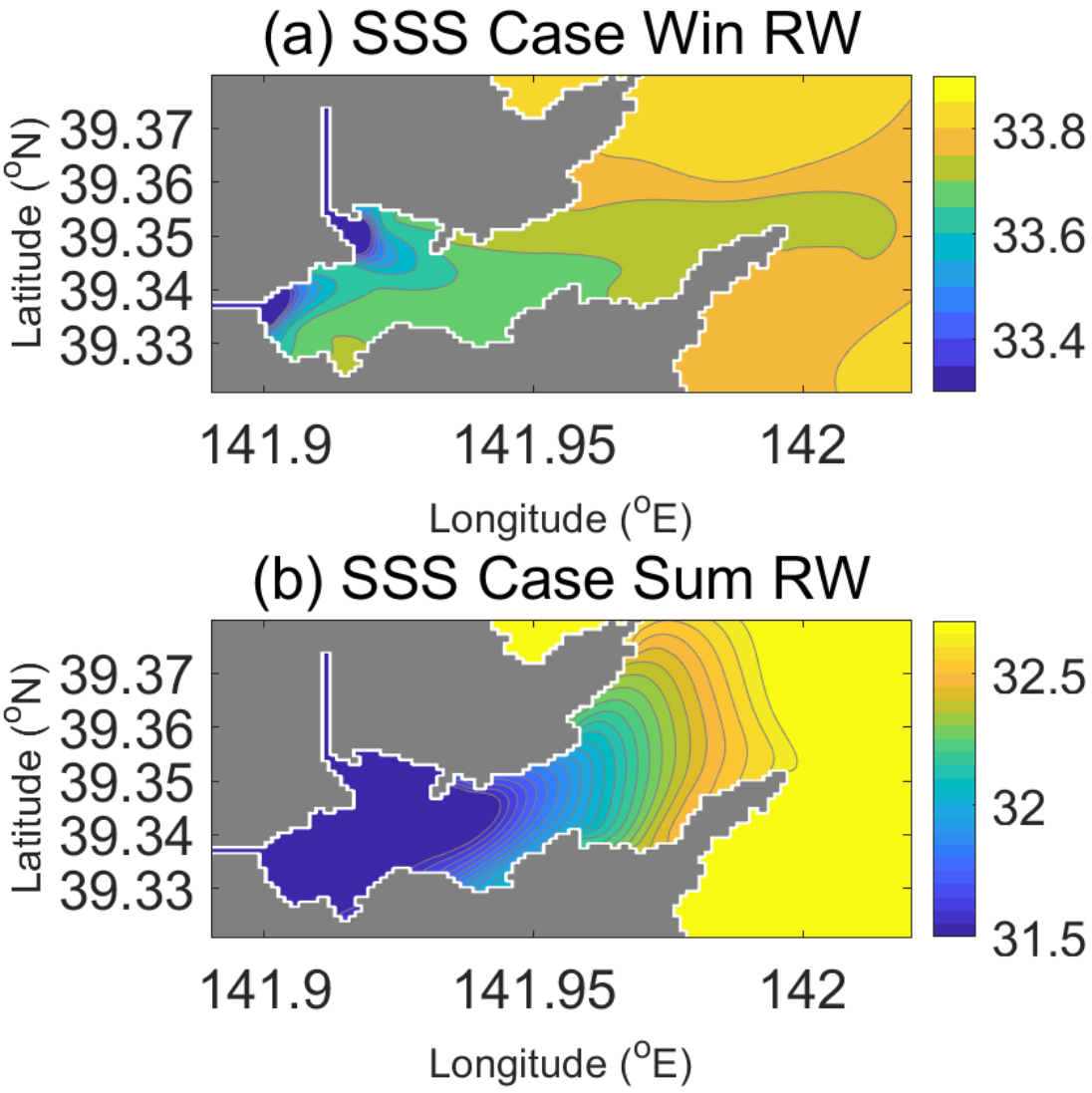

Fig.3.3-2, Same as Fig.3.3-1, but for (a) Case Win RW and (b) Case Sum RW.

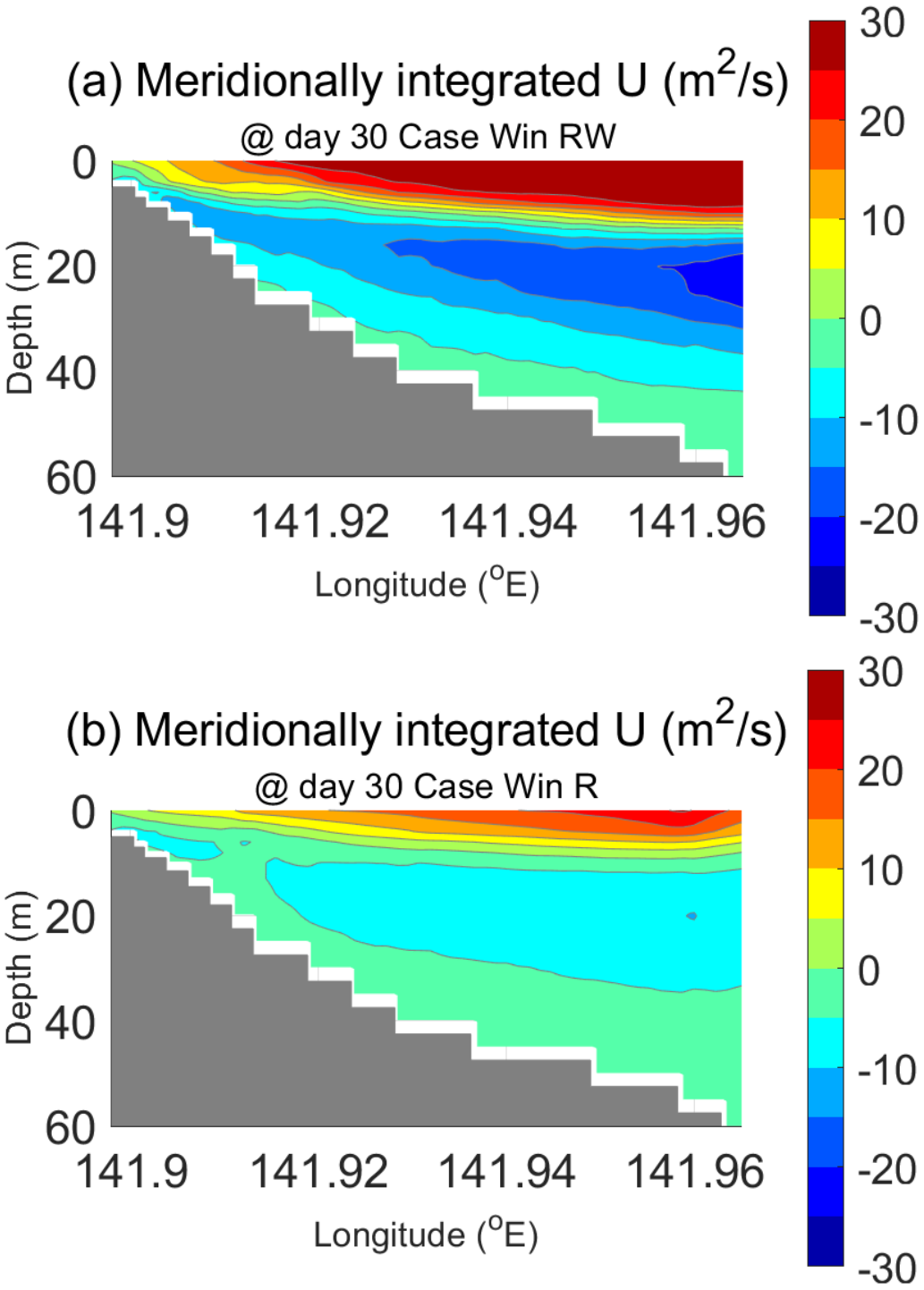

Fig.3.3-3, Zonal velocity (U) in (a) Case Win RW and (b) Case Win R that was integrated meridionally all over the bay on 30th day of numerical experiments which represent the strength of estuary circulation. The positive sign indicates outward velocity.

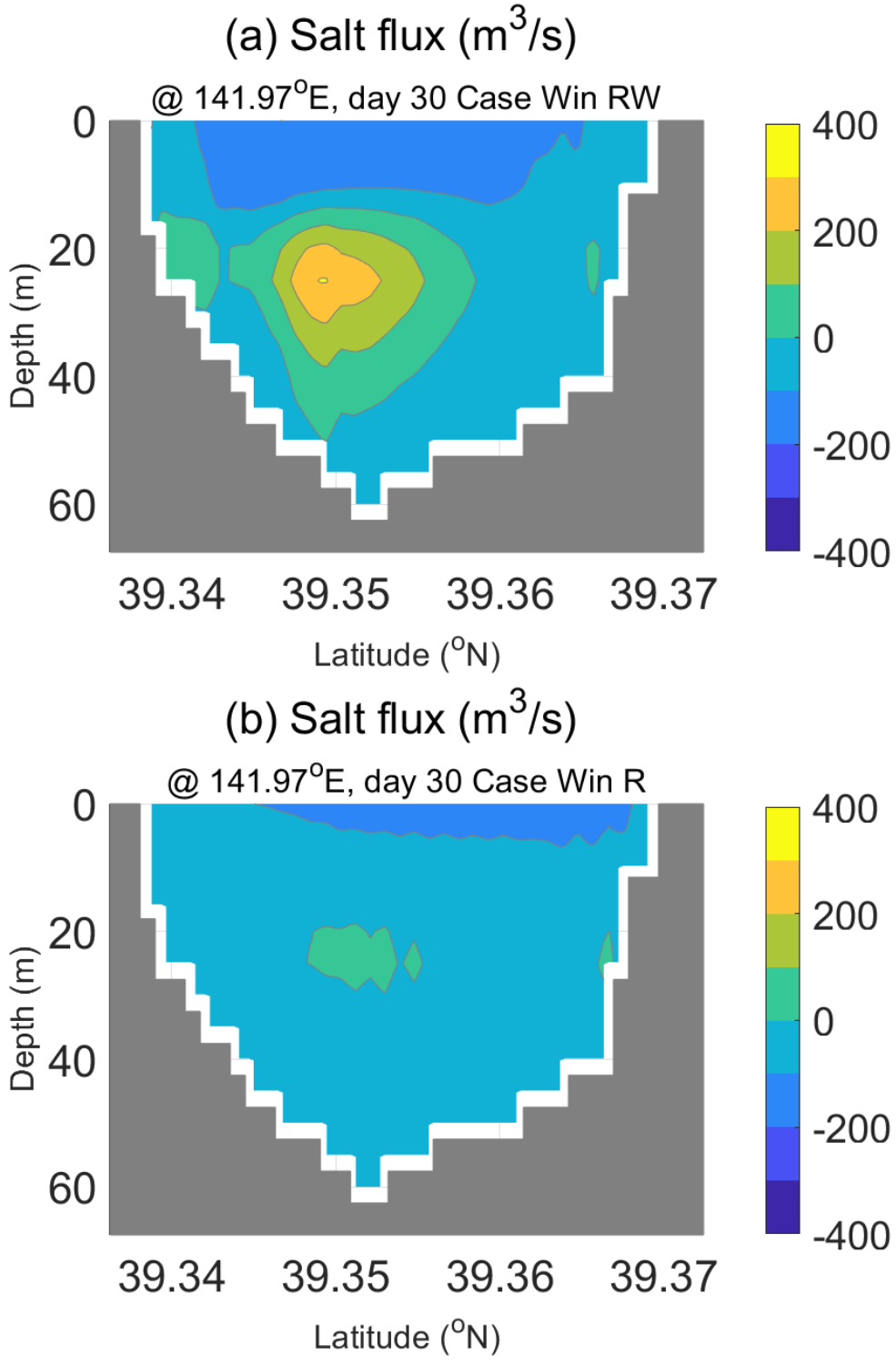

Fig.3.3-4, Salt flux at the cross section (141.97 ° E) in (a) Case Win RW and (b) Case Win R at the bay mouth on 30th day of numerical experiments.

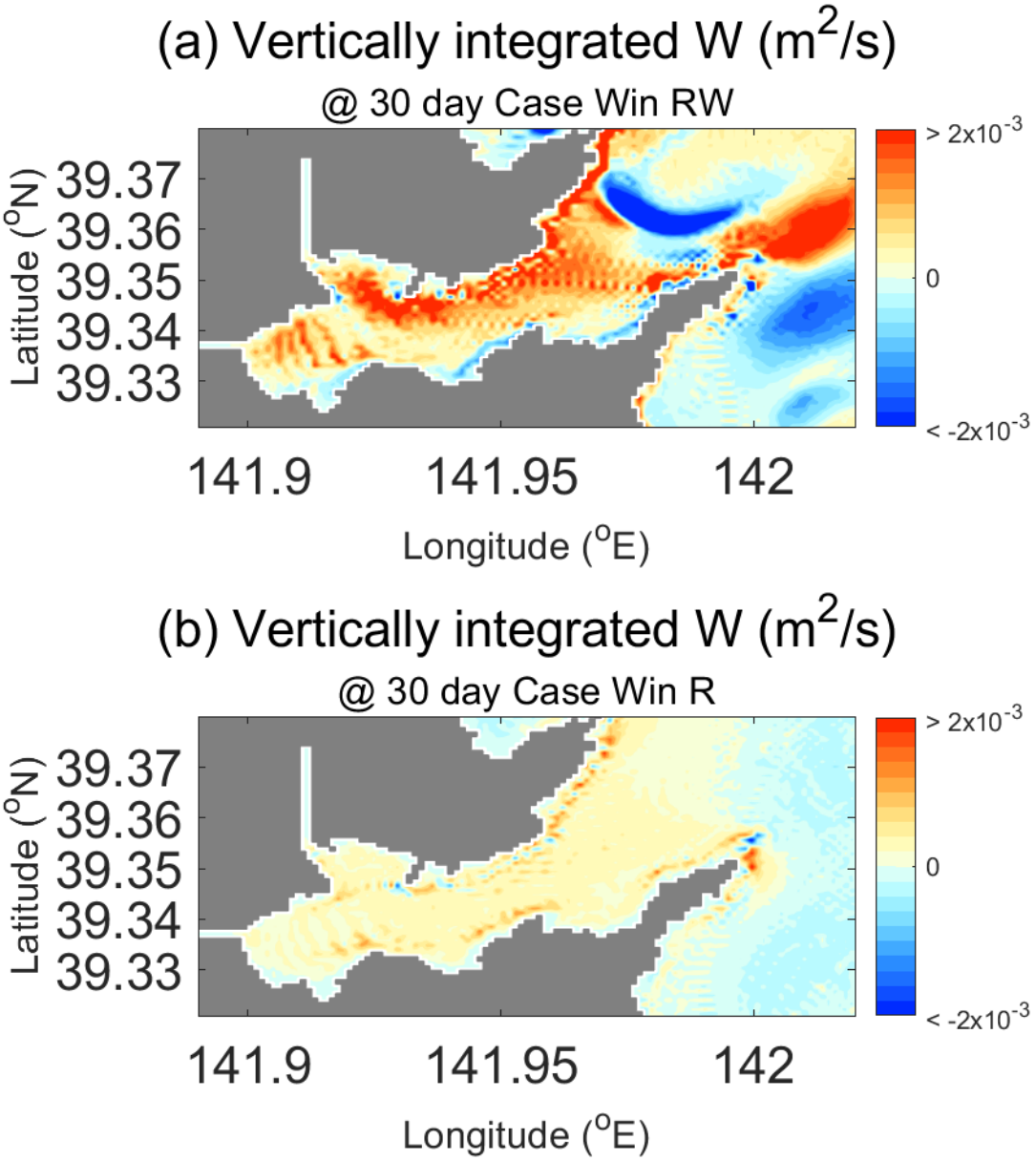

Fig.3.3-5, Upward velocity (W) in (a) Case Win RW and (b) Case Win R on 30th day of numerical experiments, after vertically integrated. Positive sign indicate upward velocity.

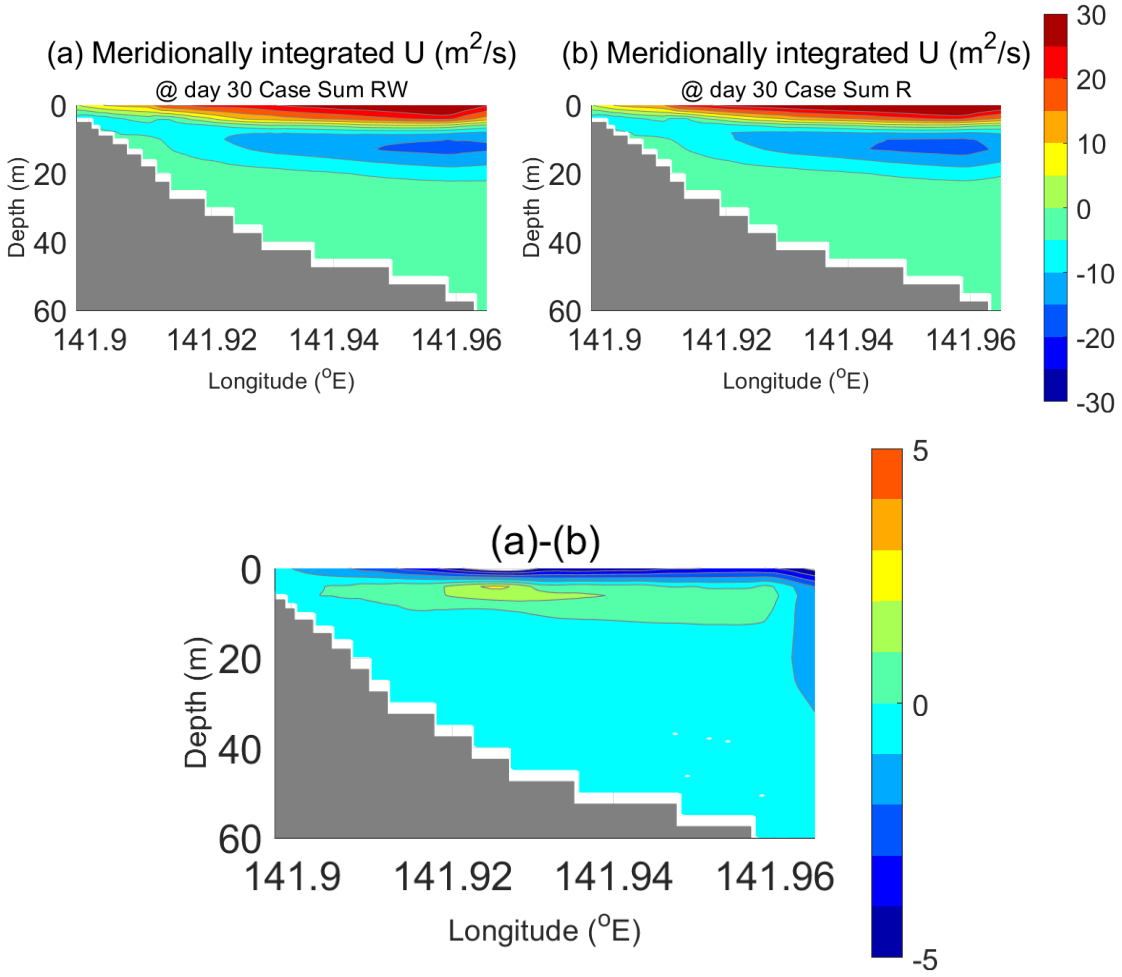

Fig.3.3-6, Same as Fig.3.2-3, but for summer cases (a) Case Sum RW and (b) Case Sum R. Lower panel indicates difference between (a) and (b).

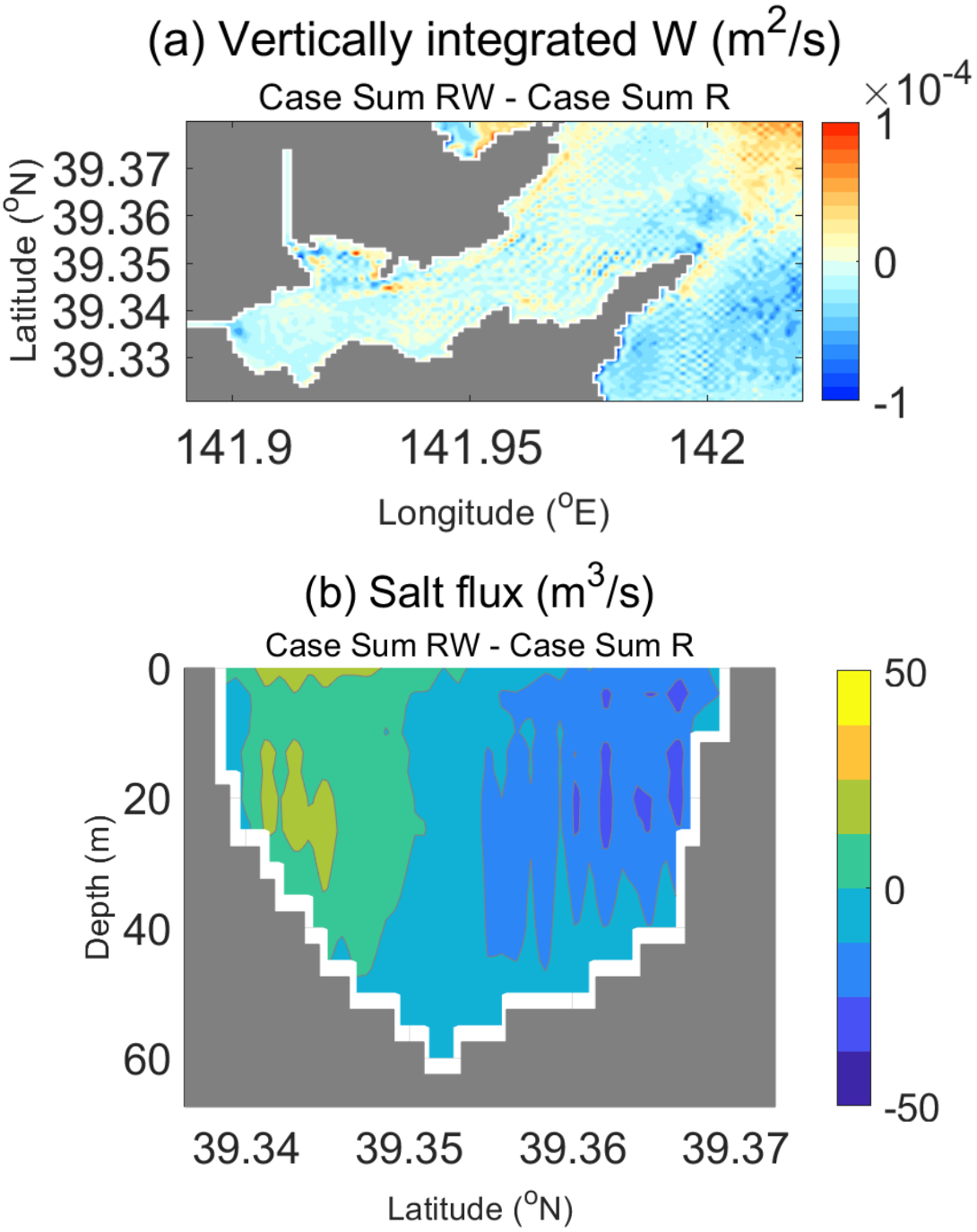

Fig.3.3-7, Difference between Case Sum RW and Case Sum R. (a) difference vertically integrated upward velocity (W) on 30th day of numerical experiments and (b) difference between salt flux at the same cross section on 30th day of numerical experiments in Fig.3.2-4.

3.4 Case study results in the numerical experiments

In section 3.3, it was found that the northwesterly wind played an important role on the positive salinity gradient pattern in Case Win RW. In this section, we comprehensively investigated the effect of the river discharge and the northwesterly wind on the circulation: We performed several numerical experiments by varying the forcings (Table.3.4-1) with the initial conditions of Case Win. The maximum of forcings in the experiments were set to the maximum forcings during winter 2015 in the observation (Fig.2.2-5 and Fig.2.2-6). The result is shown in Fig.3.4-1.

Without the effect of the northwesterly wind, the only negative salinity gradient patterns were reproduced. On the other hand, with the effect of the northwesterly wind, most of the cases reproduced the positive salinity gradient pattern. The salinity gradient tended to increase monotonously with increase in wind, and it was confirmed that the northwesterly wind plays important roles in the positive salinity gradient patterns.

In contrast, the salinity gradient did not tend to increase monotonously with increase in river discharge, indicating the maximum salinity gradient at the medium discharge of L×5. The non-monotonous tendency of the river discharge effect is explained by our hypothesis and theoretical estimation which are presented in sections 3.1 and 3.2. That is when the river discharge exceeds a certain threshold, the internal Rossby deformation radius also exceeds a threshold, resulting in the decrease in salinity gradient. Indeed, the experimental relationship between the internal deformation radius and the salinity gradient show the same tendency as in observational result (Fig.3.4-2).

Table.3.4-1, Case study forcings. NW and L indicate forcings that had been shown in Table.2.2-1. Initial conditions of winter case were used. Forcings were examined up to 10 times, which was the maximum forcings in the winter on 2015. The experiments were conducted in the cases with O.

L×10	O	O	O	O
L×5	O	O	O	O
L	Case Win R	Case Win RW	O	O
No river	-	O	-	O
Forcing	No wind	NW	NW×5	NW×10

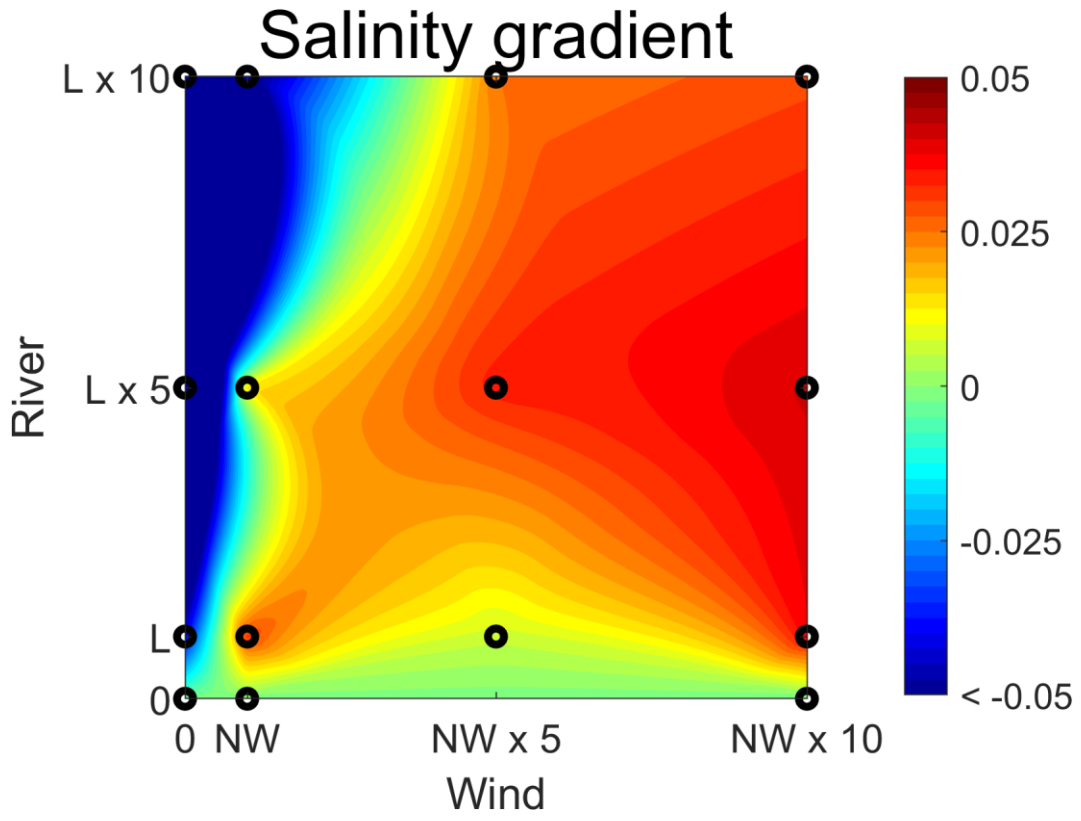

Fig.3.4-1, Salinity gradient that determined by the balance between northwesterly wind and river. Forcings in Table.3.3-1 were imposed. Black dots indicate performed numerical experiments.

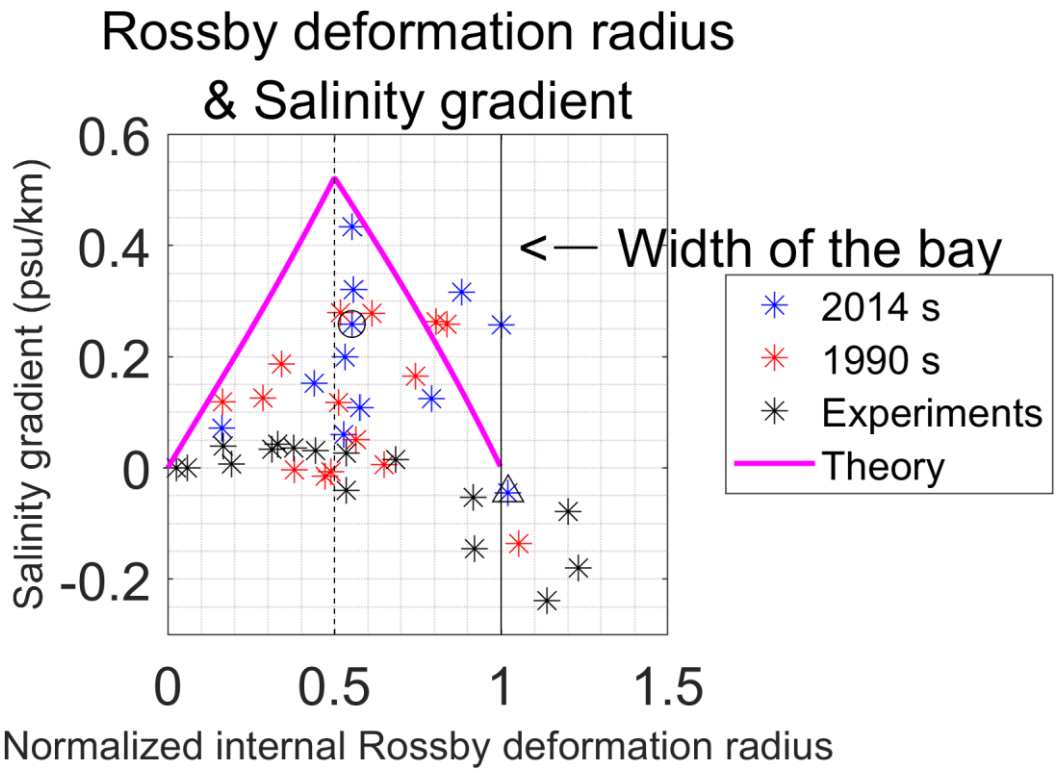

Fig.3.4-2, Internal Rossby deformation radii and salinity gradients. Blue points and red points are same as Fig.3.1-5, but with the numerical experiments results (black dots) and theoretical estimation (magenta solid line). The internal deformation radii are normalized with the width of the bay 2000 m in observation, 1700 m in numerical simulation due to 100 m resolution square grid.

4. Conclusions

We produced regularly-gridded data to draw maps of sea surface salinity that had been observed in Otsuchi Bay. To do this adequately, we applied Kuragano and Kamachi (2000) method (one of an objective analysis methods) to the data. This method can take the anisotropic spatial distribution of the observed variables into consideration. As a result, it was found that there are two typical patterns of sea surface salinity in the bay: Positive salinity gradient pattern and negative salinity gradient pattern.

According to the previous theories, river water tends to flow with the coast to the right in the northern hemisphere due to the Earth's rotation effect (e.g. Minato, 1983). This may suggest that a positive salinity gradient pattern is formed in the bay. However, a negative salinity gradient pattern sometimes occurred in the real sea. The internal Rossby deformation radius is the length scale of geostrophic adjustment due to the Earth's rotation. Therefore, the river water is generally confined within the internal Rossby deformation radius from the coast. We presented the hypothesis that the relationship between the salinity gradients and the internal Rossby deformation radii as follows: If there is no river discharge and homogenous, there must be zero salinity gradient, as well as, the zero internal Rossby deformation radius. As river discharge increase from zero, it will form or strengthen the stratification and the internal deformation radius would also increase. Consequently, the salinity gradient will increase. However, as the internal Rossby deformation radius exceeds a certain threshold, the salinity gradient will start to decrease. Indeed, the large positive values of the salinity gradient were observed in the medium range of the internal Rossby deformation radius between 1000 m and 2000 m. Moreover, large negative values of the salinity gradient were observed when the internal Rossby deformation radius was larger than 2000 m, which is the width of the bay. The increasing and decreasing salinity gradient with respect to the internal Rossby deformation radii in the observation may be explained by the presented theory of river water spread. However, a large variance existed in the relation between the deformation radius and the salinity gradient. This large variance implies that the salinity distribution may be determined not only by the river discharge, but also by another factor.

Another factor that we focused on was the wind. We performed numerical experiments to investigate the effects of the winds on the circulation on November 6th, 2015, and that on June 26th, 2014. In the winter case (positive salinity gradient pattern on November 6th, 2015), the northwesterly wind was imposed. The northwesterly wind intensified estuary circulation that is associated with increased salt flux from the Pacific, as suggested in previous studies based on the observational data (Otobe et al., 2009; Ishizu et al. 2017). Moreover, the upwelling and downwelling were strengthened

on the northern and southern coasts, respectively by the wind and the positive gradient pattern was successfully reproduced. This result indicates the northwesterly wind played important roles in the formation of the positive salinity gradient pattern. It should be noted that northwesterly wind occupies about 75% of all the winds in the bay (2015, Fig.2.2-6), which suggests the importance of the northwesterly wind in the circulation in the real sea.

In contrast, in the summer cases (negative salinity gradient pattern on June 26th, 2014), there was no large difference in the circulation between without and with the southeasterly wind, unlike the salinity gradient. This implies that the wind generates the large variance in the salinity gradient.

Finally, we comprehensively investigated the effect of the river discharge and the northwesterly wind on the circulation. The salinity gradient tended to increase monotonously with the increase in wind, and it was confirmed that the northwesterly wind plays important roles in the positive salinity gradient pattern. In contrast, the salinity gradient did not tend to increase monotonously with the increase in river discharge, and the non-monotonous tendency of the river discharge effect is explained by our hypothesis.

In this study, we investigated the effects of river discharge, the Earth's rotation effect, and wind on the salinity gradient pattern with monthly forcings. Schematic figures of salinity gradient formation mechanisms are shown in Fig.4-1, which are inferred in this study. With the northwesterly wind, estuary circulation and associated salt flux from the Pacific are reinforced. Moreover, the upwelling is strengthened on the northern coast. Therefore, high-salinity water from the sub-surface is transported to the surface. As a result, the positive salinity gradient pattern is generated with the smaller internal Rossby deformation radius compared to the width of the bay. On the other hand, the negative salinity gradient pattern is generated with the larger internal Rossby deformation radius compared to the width of the bay. Although the southeasterly wind slightly changed the circulation, it may not be important compared to northwesterly winds, and the asymmetric effects of the winds on the circulation might be a cause of the large variance in the relation between the internal deformation radius and the salinity gradient. In reality, the salinity gradient pattern could be influenced by other mechanisms that were not discussed in this study. We aim to investigate such mechanisms, for example, tide and internal tide in the near future.

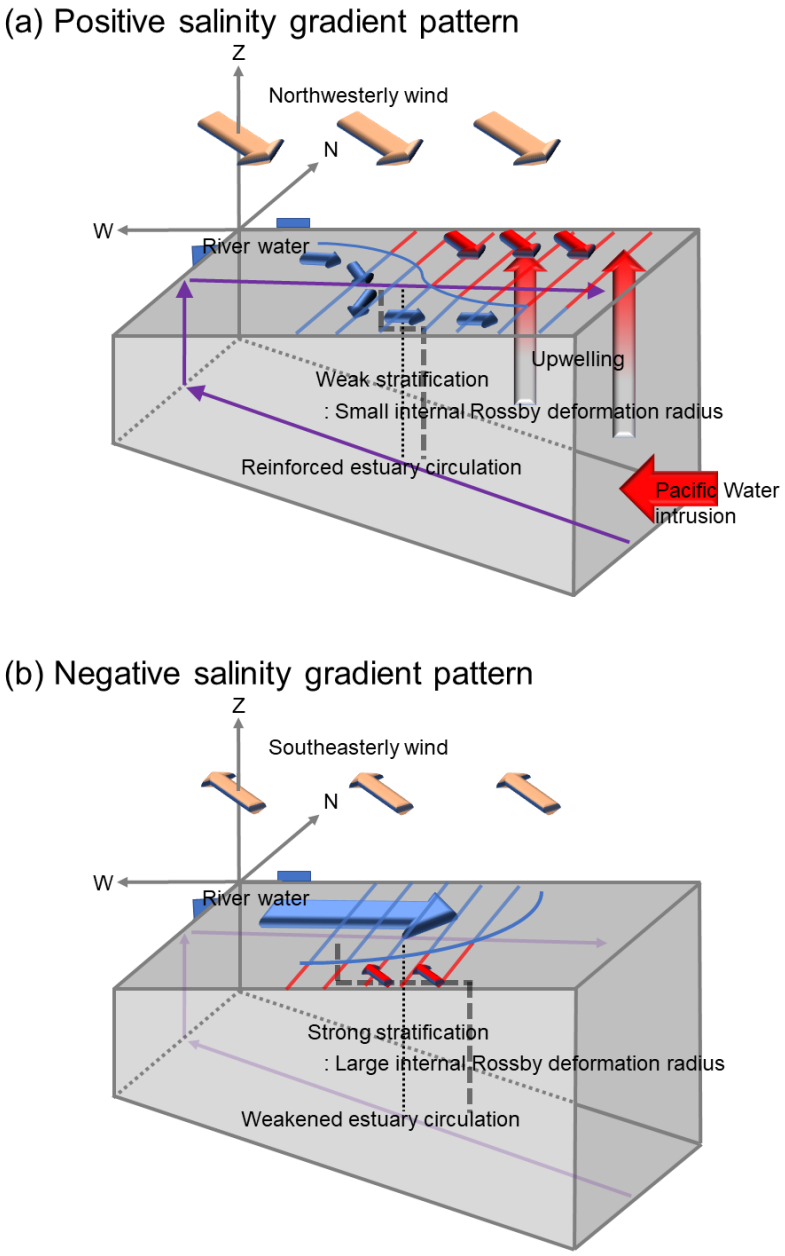

Fig.4-1, Schematic figures of salinity gradient formation mechanisms. The positive and negative salinity gradient pattern are shown in (a) and (b), respectively.

Acknowledgement

I am deeply indebted to my supervisor, Tanaka, K. for valuable advice and patient encouragement.

I express my gratitude to Komatsu, K., Kutsuwada, K., and Y. Minegishi for providing valuable in-situ observed CTD data. Also, I express my gratitude to Sakamoto, T. T., and Hasumi, H. for the valuable advice for CCSR Ocean Component Model version 4.0. Usage of high-resolution observed data and numerical experiments were important parts of this study.

I express my gratitude again to Adachi, T. for providing the river data, and Komatsu, T. for providing the bathymetric data of Otsuchi Bay. The bathymetric data of the Sanriku ria coast were provided by Japan Oceanographic Data Center. The offshore CTD observation data were provided by the Iwate Fisheries Technology Center. The wind and precipitation data were provided by Japan Meteorological Agency.

I would like to thank all past and present members of the Ocean Physics and Climate Dynamics Seminar for their insightful suggestions and critical comments. Moreover, I thank all past and present members of the physical oceanography student room 621 for their valuable comments and help.

I would like to thank Park, J. H., and Hibiya, T. that helping and encouraging me to start studying physical oceanography. I would like to thank Kido, S., Murata, K., Kusumi, T., and Sasaki, Y. for helping me to settle well to studying in Japan. I would like to thank Song, S. Y., Jeong, J. S., and other members of our study group (International Climate and Ocean science meeting) for valuable discussions.

I would like to acknowledge the financial support of World-leading Innovative Graduate Study Program in Proactive Environmental Studies (WING-PES), University of Tokyo.

Finally, I would like to express my gratitude to my family, and Kim, J. for their warm support.

References

安保 綾子 ・乙部 弘隆 ・高木 稔 (2005) : 大槌湾に流入する河川水. 東京大学海洋研究所国際沿岸海洋研究センター編, 30:4-8

Bretherton, F. P., Davis, R. E., and Fandry, C. B. (1976) : A technique for objective analysis and design of oceanographic experiments applied to MODE-73. Deep-sea research, 23: 559-582

Cushman-Roisin, B., and Beckers, J. M. (2011) : Introduction to geophysical fluid dynamics: physical and numerical aspect. Academic press

Furuya, K., Takahashi, K., and Izumi, H. (1993) : Wind-dependent formation of phytoplankton spring bloom in Otsuchi Bay, a ria in Sanriku, Japan. Journal of oceanography, 49: 459-475

Gill, A. E. (1982) : Atmosphere-ocean dynamics. Academic press

Hasumi, H. (2006) : CCSR Ocean Component Model (COCO) version 4.0. CCSR Report 25

Ishizu, M., Itoh, S., Tanaka, K., and Komatsu, K. (2017) : Influence of the Oyashio Current and Tsugaru Warm Current on the circulation and water properties of Otsuchi Bay, Japan. Journal of oceanography, 73: 115-131

Johnson, H. K. (1999) : Simple expressions for correcting wind speed data for elevation. Coastal Engineering, 36: 263-269

Kawamiya, M., Kishi, M. J., Ahmed, M. D. K., and Sugimoto, T. (1996) : Causes and consequences of spring phytoplankton blooms in Otsuchi Bay, Japan. Continental shelf research, 16: 1683-1698

Kishi, M. J., Hisashi, N., Takagi, M., Sekiguchi, K., Otobe, H., Furuya, K., and Aiki, T. (2003) : Effect of aquaculture on material cycles in Otsuchi Bay, Japan. Otsuchi marine science, 28: 65-71

Knauss, J. A. (1978) : Introduction to physical oceanography. Prentice-Hall

Kuragano, T., and Kamachi, M. (2000) : Global statistical space-time scales of oceanic variability estimated from the TOPEX/POSEIDON altimeter data. Journal of geophysical research, 105: 955-974

Lentz, S. J., Helfrich, K. R. (2002) : Bouyant gravity current along a sloping bottom in a rotating fluid. Journal of fluid mechanic, 464: 251-278

Masunaga, E., Fringer, O. B., and Yamazaki, H. (2016) : An observational and numerical study of river plume dynamics in Otsuchi Bay, Japan. Journal of oceanography, 72: 3-21

Minato, S. (1983) : Geostrophic response near the coast. Journal of oceanography, 39: 141-149

Mizuno, K. (1995) : Basin-scale hydrographic analysis and optimal interpolation method. 海の研究, 4: 187-208

Noh, Y., Kim, H. J. (1999) : Simulations of temperature and turbulence structure of the oceanic

boundary layer with the improved near-surface process. Journal of geophysical research, 104: 15621-15634

Otobe, H., Onishi, H., Inada, M., Michida, Y., and Terazaki, M. (2009) : Estimation of water circulation in Otsuchi Bay, Japan inferred from ADCP observation. Coastal marine science, 33(1): 000-000

Rosati, A., and Miyakoda, K. (1988) : A general circulation model for upper ocean simulation. Journal of physical oceanography, 18: 1601-1626

Sakamoto, T. T., Urakawa, S., Hasumi, H., Ishizu, M., Itoh, S., Komatsu, T., and Tanaka, K. (2017) : Numerical simulation of Pacific water intrusions into Ostuchi Bay, northeast of Japan, with a nested-grid OGCM. Journal of oceanography, 73: 39-54

Sasmal, K., Masunaga, E., Webb, A., Fringer, O. B., Gross, E. S., Rayson, M. D., and Yamazaki, H. (2018) : A three-dimensional numerical study of river plume mixing process in Otsuchi Bay, Japan. Journal of oceanography, 74: 169-186

Smagorinsky, J. (1963) : General circulation experiments with the primitive equations. Monthly weather review, 91: 99-164

Tanaka, K., Michida, Y., and Komatsu, T. (2008) : Numerical experiments on wind-driven circulations and associated transport processes in Suruga Bay. Journal of oceanography, 64: 93-102

Tanaka, K., Komatsu, K., Itoh, S., Yanagimoto, D., Ishizu, M., Hasumi, H., Sakamoto, T., Urakawa, S., and Michida, Y. (2017) : Baroclinic circulation and its high frequency variability in Otsuchi Bay on the Sanriku ria coast, Japan. Journal of oceanography, 73: 25-38

Vallis, G. K. (2006) : Atmosphere and oceanic fluid dynamics. Cambridge university press

Yankovsky, A. E., and Chapman, D. C. (1997) : A simple theory for the fate of buoyant coastal discharge. Journal of physical oceanography, 27: 1386-1401

Appendix

A.2.1-1, Detailed information on CTD observations conducted in the Otsuchi Bay.

Table.A.2.1-1-1, CTD observation stations and observed day (YY/MM/DD) from 1990 to 1991. Light blue colored boxes with "O" indicate conducted observation and light red colored boxes with "-" indicate missing observation.

	Long. (oE)	Lat. (oN)	90 01 16	90 02 19	90 03 12	90 04 18	90 05 14	90 06 13	90 07 12	90 08 13	90 09 12	90 10 11	90 11 20	90 12 18	91 01 16	91 02 14	91 03 19
r1	141.9903	39.3562	O	-	O	-	O	O	-	O	O	O	O	O	O	O	O
r2	141.9838	39.3634	O	-	O	-	O	O	-	O	O	O	O	O	O	O	O
r3	141.9737	39.3714	O	-	O	-	O	O	-	O	O	O	O	O	O	O	O
r4	141.9597	39.3561	O	O	O	O	O	O	-	O	O	-	-	-	-	-	-
r5	141.9618	39.3555	O	O	-	-	-	O	O	O	O	-	-	-	-	-	-
r6	141.9650	39.3541	O	O	O	O	O	O	O	O	O	-	-	-	-	-	-
r7	141.9674	39.3515	O	O	O	O	O	O	O	O	O	-	-	-	-	-	-
r8	141.9705	39.3484	O	O	O	O	O	O	-	O	O	-	-	-	-	-	-
r9	141.9712	39.3435	O	O	O	O	O	O	O	O	O	-	-	-	-	-	-
r10	141.9711	39.3401	O	O	O	O	O	O	O	O	O	-	-	-	-	-	-
r11	141.9478	39.3377	-	O	O	O	O	O	O	O	O	O	O	O	O	O	O
r12	141.9469	39.3408	-	O	O	O	O	O	O	O	O	O	O	O	O	O	O
r13	141.9443	39.3429	-	O	O	O	O	O	O	O	O	O	O	O	O	O	O
r14	141.9418	39.3454	-	O	O	O	O	O	O	O	O	O	O	O	O	O	O
r15	141.9398	39.3473	-	O	O	O	O	O	O	O	O	O	O	O	O	O	O
r16	141.9317	39.3467	O	-	-	-	-	-	-	-	-	-	-	-	-	-	-
r17	141.9331	39.3450	O	-	-	-	-	-	-	-	-	-	-	-	-	-	-
r18	141.9344	39.3429	O	-	-	-	-	-	-	-	-	-	-	-	-	-	-
r19	141.9360	39.3410	O	-	-	-	-	-	-	-	-	-	-	-	-	-	-
r20	141.9382	39.3381	O	-	-	-	-	-	-	-	-	-	-	-	-	-	-
r21	141.9398	39.3355	O	-	-	-	-	-	-	-	-	-	-	-	-	-	-
r22	141.9412	39.3335	O	-	-	-	-	-	-	-	-	-	-	-	-	-	-

Table.A.2.1-1-1 (continued)

	Long. (oE)	Lat. (oN)	90 01 16	90 02 19	90 03 12	90 04 18	90 05 14	90 06 13	90 07 12	90 08 13	90 09 12	90 10 11	90 11 20	90 12 18	91 01 16	91 02 14	91 03 19
r23	141.9302	39.3465	-	-	-	-	-	-	-	-	-	O	O	O	O	O	O
r24	141.9285	39.3440	-	-	-	-	-	-	-	-	-	O	O	O	O	O	O
r25	141.9270	39.3414	-	-	-	-	-	-	-	-	-	O	O	O	O	O	O
r26	141.9251	39.3380	-	-	-	-	-	-	-	-	-	O	O	O	O	O	O
r27	141.9235	39.3344	-	-	-	-	-	-	-	-	-	O	O	O	O	O	O
r28	141.9167	39.3444	O	O	O	O	O	O	O	O	O	O	O	O	O	O	-
r29	141.9172	39.3431	O	O	O	O	O	O	O	O	O	O	O	O	O	O	-
r30	141.9181	39.3410	O	O	O	O	O	O	O	O	O	O	O	O	O	O	-
r31	141.9189	39.3389	O	O	O	O	O	O	O	O	O	O	O	O	O	O	-
r32	141.9200	39.3372	O	O	O	O	O	O	O	O	O	O	O	O	O	O	-
r33	141.9214	39.3351	O	O	O	O	O	O	O	O	O	O	O	O	O	O	-
r34	141.9103	39.3300	O	-	-	O	O	O	O	O	O	O	O	O	O	O	-
r35	141.9097	39.3318	O	-	-	O	O	O	O	O	O	-	O	O	O	O	O
r36	141.9098	39.3341	O	-	-	O	O	O	O	O	O	O	O	O	O	O	O
r37	141.9081	39.3360	O	-	-	O	O	O	O	O	O	-	O	O	O	O	O
r38	141.9075	39.3383	O	-	-	O	O	O	O	O	O	O	O	O	O	O	O
r39	141.9073	39.3404	O	-	-	O	O	O	O	O	O	O	O	O	O	O	O
r40	141.9162	39.3483	O	O	-	O	O	O	O	O	O	O	O	O	O	O	O
r41	141.9175	39.3492	O	O	O	O	O	O	O	O	O	-	O	O	O	O	O
r42	141.9188	39.3500	O	O	O	O	O	O	O	O	O	O	O	O	O	O	O
r43	141.9196	39.3512	O	O	O	O	O	O	O	O	O	-	O	O	O	O	O
r44	141.9209	39.3523	O	O	O	O	O	O	O	O	O	O	O	O	O	O	O

Table.A.2.1-1-2, Same as Table.A.2.1-1-1, but for observation from 2014 to 2015.

	Long. (°E)	Lat. (°N)	14 06 26	14 07 28	14 10 30	15 02 16	15 03 17	15 04 23	15 05 27	15 06 12	15 06 24	15 07 07	15 07 22	15 08 19	15 09 03	15 10 23	15 11 06
b1	141.9790	39.3484	O	O	O	O	O	O	O	O	O	O	O	-	O	-	O
b2	141.9778	39.3493	O	O	O	O	O	O	O	O	O	O	O	-	O	-	O
b3	141.9752	39.3519	O	O	O	O	O	O	O	O	O	O	O	-	O	-	O
b4	141.9722	39.3541	O	O	O	O	O	O	O	O	O	O	O	-	O	-	O
b5	141.9693	39.3566	O	O	O	O	O	O	O	O	O	O	O	-	O	-	O
b6	141.9680	39.3579	O	O	O	O	O	O	O	O	O	O	O	-	O	-	O
b7	141.9632	39.3619	O	O	O	O	O	O	O	O	O	O	O	-	O	-	O
b8	141.9488	39.3493	O	O	O	O	O	O	O	O	O	O	O	O	O	-	O
b9	141.9529	39.3483	O	O	O	O	O	O	O	O	O	O	O	O	O	-	O
b10	141.9557	39.3467	O	O	O	O	O	O	O	O	O	O	O	O	O	-	O
b11	141.9585	39.3450	O	O	O	O	O	O	O	O	O	O	O	O	O	-	O
b12	141.9610	39.3435	O	O	O	O	O	O	O	O	O	O	O	O	O	-	O
b13	141.9495	39.3403	O	O	O	O	O	O	O	O	O	O	O	O	O	-	O
b14	141.9480	39.3421	O	O	O	O	O	O	O	O	O	O	O	O	O	-	O
b15	141.9464	39.3435	O	O	O	O	O	O	O	O	O	O	O	O	O	-	O
b16	141.9439	39.3448	O	O	O	O	O	-	O	O	O	O	O	O	O	-	O
b17	141.9411	39.3463	O	O	O	O	O	-	O	O	O	O	O	O	O	-	O
b18	141.9332	39.3463	O	O	O	O	O	-	O	O	O	O	O	O	O	O	O
b19	141.9344	39.3443	O	O	O	O	O	-	O	O	O	O	O	O	O	-	O
b20	141.9361	39.3415	O	O	O	O	O	-	O	O	O	O	O	O	O	-	O
b21	141.9374	39.3389	O	O	O	O	O	-	O	O	O	O	O	O	O	-	O
b22	141.9388	39.3360	O	O	O	O	O	-	O	O	O	O	O	O	O	-	O
b23	141.9392	39.3350	O	O	O	O	O	-	O	O	O	O	O	O	O	O	O
b24	141.9359	39.3371	-	O	O	O	O	-	O	O	O	O	O	O	O	-	O
b25	141.9341	39.3389	O	O	O	O	O	-	O	O	O	O	O	O	O	-	O
b26	141.9302	39.3413	O	O	O	O	O	-	O	O	O	O	O	O	O	O	O
b27	141.9277	39.3427	O	O	O	O	O	-	O	O	O	O	O	O	O	-	O

Table.A.2.1-1-2 (continued)

b28	141.9254	39.3445	O	O	O	O	O	-	O	O	O	O	O	O	O	-	O
b29	141.9213	39.3473	O	O	O	O	O	-	O	O	O	O	O	O	O	-	O
b30	141.9181	39.3491	O	O	O	O	O	-	O	O	O	O	O	O	O	O	O
b31	141.9094	39.3404	O	O	O	O	O	-	O	O	O	O	O	O	O	O	O
b32	141.9119	39.3377	O	O	O	O	O	-	O	O	O	O	O	O	O	-	O
b33	141.9140	39.3366	O	O	O	O	O	-	O	O	O	O	O	O	O	O	O
b34	141.9149	39.3322	O	O	O	O	O	-	O	O	O	O	O	O	O	-	O
b35	141.9158	39.3303	O	O	O	O	O	-	O	O	O	O	O	O	O	O	O
b36	141.9038	39.3284	O	O	O	O	O	-	O	O	O	O	O	O	O	O	O
b37	141.9021	39.3322	O	O	O	O	O	-	O	O	O	O	O	O	O	-	O
b38	141.9014	39.3333	O	O	O	O	O	-	O	O	O	O	O	O	O	O	O
b39	141.9010	39.3359	O	O	O	O	O	-	O	O	O	O	O	O	O	-	O
b40	141.9012	39.3376	O	O	O	O	O	-	O	O	O	O	O	O	O	O	O
b41	141.9243	39.3459	O	-	-	O	O	-	O	O	O	O	O	O	O	O	O
b42	141.9210	39.3477	-	-	-	O	O	-	O	O	O	O	O	O	O	O	O

Table.A.2.1-1-3, Same as Table.A.2.1-1-1, but for observation from 2018 to 2019.

	Long. (°E)	**Lat. (°N)**	**14 06 26**	**14 07 28**	**14 10 30**	**15 02 16**	**15 03 17**	**15 04 23**	**15 05 27**	**15 06 12**	**15 06 24**	**15 07 07**	**15 07 22**	**15 08 19**	**15 09 03**	**15 10 23**	**15 11 06**
k1	141.9008	39.3336	O	O	O	O	O	O	O	O	O	O	O	O	O	O	O
k2	141.9145	39.3374	O	O	O	O	O	O	O	O	O	O	O	O	O	O	O
k3	141.9146	39.3299	O	O	O	O	O	O	O	O	O	O	O	O	O	O	O
k4	141.9690	39.3701	O	O	O	O	O	O	O	O	O	O	-	O	O	-	O
k5	141.9892	39.3511	O	O	O	O	O	-	O	O	O	O	-	O	O	-	O
k6	141.9391	39.3400	-	O	O	O	O	O	O	O	O	O	O	O	O	O	O
k7	141.9253	39.3394	O	O	O	O	O	O	O	O	O	O	O	O	O	O	O
k8	141.9901	39.3631	O	O	O	O	O	-	O	O	O	O	-	O	O	O	O
k9	142.0097	39.3705	-	-	-	-	-	-	-	-	-	-	-	-	-	-	-

Table.A.2.1-1-3 (continued)

		14 06 26	14 07 28	14 10 30	15 02 16	15 03 17	15 04 23	15 05 27	15 06 12	15 06 24	15 07 07	15 07 22	15 08 19	15 09 03	15 10 23	15 11 06
k1	O	O	O	O	O	O	O	O	O	O	O	O	O	O	O	O
k2	O	O	O	O	O	O	O	O	O	O	O	O	O	O	O	O
k3	O	O	O	O	O	O	O	O	O	O	O	O	O	O	O	O
k4	-	O	O	O	-	O	O	O	O	O	O	O	O	O	-	O
k5	-	O	O	O	-	O	O	O	O	O	O	-	O	O	-	O
k6	O	O	O	O	O	O	O	O	O	O	O	O	O	O	O	O
k7	O	O	O	O	O	O	O	O	O	O	O	O	O	O	O	O
k8	-	O	O	O	-	O	O	O	O	O	O	-	O	O	-	O
k9	-	-	-	-	-	O	O	O	O	O	-	-	O	O	-	O

A.2.1-2, Detailed procedure of objective analysis

Let P as property (e.g., temperature, salinity, density, etc.). Then the objective analysis for true value (P_z^t) in the random place (or grid) z is

$$P_z^t = M + \epsilon_z = \Sigma_{i=1}^n w_i P_i^o \quad \text{(A.2.1-2.1)}$$

$$\text{when} \quad \Sigma_{i=1}^n w_i = 1 \quad \text{(A.2.1-2.2)}$$

where, M is mean value, P_i^o is observed value in ith observation station among nth observations, and w_i is the optimal weight (Bretherton et al., 1976) in random place z. According to Bretherton et al. (1976), constraint ($\Sigma_{i=1}^n w_i = 1$) of equation (A.2.1-2.2) is needed for zero bias ($\overline{(P_z^t)} = \overline{(P_i^o)}$) estimation of true value (P_z^t).

The goal is to find the optimal weight w_i which minimizes the error (I_z). The optimal weight w_i is calculated by linear systems of following equation.

$$\Sigma_{i=1}^n \mu_{i,j} w_j + w_i \lambda^2 + \psi = \mu_{z,i} \quad \text{(A.2.1-2.3)}$$

Where μ is a correlation function, $\mu_{i,j}$ is the correlation between the ith and jth observation stations, $\mu_{z,i}$ is the correlation between random place z and ith observed stations, and $\lambda^2 = \sigma_e^2/\sigma^2$, the variance of error over variance, which is reciprocal of signal to noise ratio. According to Mizuno (1995), equation A.2.1-2.3 can be solved as systems of linear equations.

$$\begin{bmatrix} \mu_{1,1}+\lambda^2 & \mu_{1,2} & \cdots & \mu_{1,n} & 1 \\ \mu_{2,1} & \mu_{2,2}+\lambda^2 & & & 1 \\ \vdots & & \ddots & & \vdots \\ \mu_{n,1} & & & \mu_{n,n}+\lambda^2 & 1 \\ 1 & 1 & \cdots & 1 & 0 \end{bmatrix} \begin{bmatrix} w_1 \\ w_2 \\ \vdots \\ w_n \\ \psi \end{bmatrix} = \begin{bmatrix} \mu_{z,1} \\ \mu_{z,2} \\ \vdots \\ \mu_{z,n} \\ 1 \end{bmatrix}$$

With the optimum weight w_i, error E^2 can be estimated.

$$E^2 = \Sigma_{n=1}^n \mu_{z,i} w_i + \psi. \quad \text{(A.2.1-2.4)}$$

This objective analysis method is also called as ordinary kriging. This method assumes the existence of one global mean value which spatially unchanged by constraint imposing equation A.2.1-2.2: $\Sigma_{i=1}^n w_i = 1$.

A.2.1-3, Comparison between objective analysis methods.

In this study, we produced regularly-gridded data to draw maps of sea surface salinity that had been observed in Otsuchi Bay by applying Kuragano and Kamachi (2000) method. Because statistical relationship has directional dependency (anisotropic) in Otsuchi Bay: The correlations among sea surface salinity were higher in the along-bay directions compared to the cross-bay directions (Fig. 2.1-2).

In this appendix, we compared the effect of two methods: The anisotropic and isotropic methods. First, isotropic correlation function was obtained with same method, and it is

$$\mu^o = e^{\alpha_1 (x^2 + y^2) + \alpha_2} \tag{A.2.1-3.1}$$

where, x and y are longitudinal distance and latitudinal distances. The last coefficient α_2 is related to signal to noise ratio (λ), which is

$$\frac{1}{\lambda} = \frac{\sigma^t}{\sigma^e} = \sqrt{\frac{e^{\alpha_2}}{1 - e^{\alpha_2}}} \ . \tag{A.2.1-3.2}$$

The coefficients, α_1 and $\alpha_2$were estimated to be -0.021 and -0.172, respectively. Fig.A.2.1-3-1 shows the difference between the anisotropic method and the isotropic method for the positive salinity gradient pattern on November 6th, 2015. As shown in Fig.A.2.1-3-1, the isotropic method smoothens the salinity gradient. Moreover, observed sea surface salinity distribution (colored in magenta box) was distorted more in the isotropic method compared to the anisotropic method.

As a next step, we compared the salinity gradients from 2014 to 2015 (Fig.A.2.1-3-2). Here, the OBS was defined by the gradient between the spatial averaged sea surface salinity in north stations (8, 9, 16, and 17 in Fig.2.1-1) and southern stations (11, 12, 13, and 14 in Fig.2.1-1). As shown in Fig.A.2.1-3-2, both methods smoothen the salinity gradients. This is because the objective analysis method considers general distributions of the salinity by optimal weight (in A.2.1-2). Since smoothing is related to the shape of the correlation function, the isotropic method tends to smoothen the meridional salinity gradient more compared to the anisotropic method. As a result, the residual salinity gradient between OBS and each method was generally larger in the isotropic method, which might lead to a misunderstanding of the river water spread. Therefore, we conclude that the anisotropic method (Kuragano and Kamachi, 2000) is appropriate for our study.

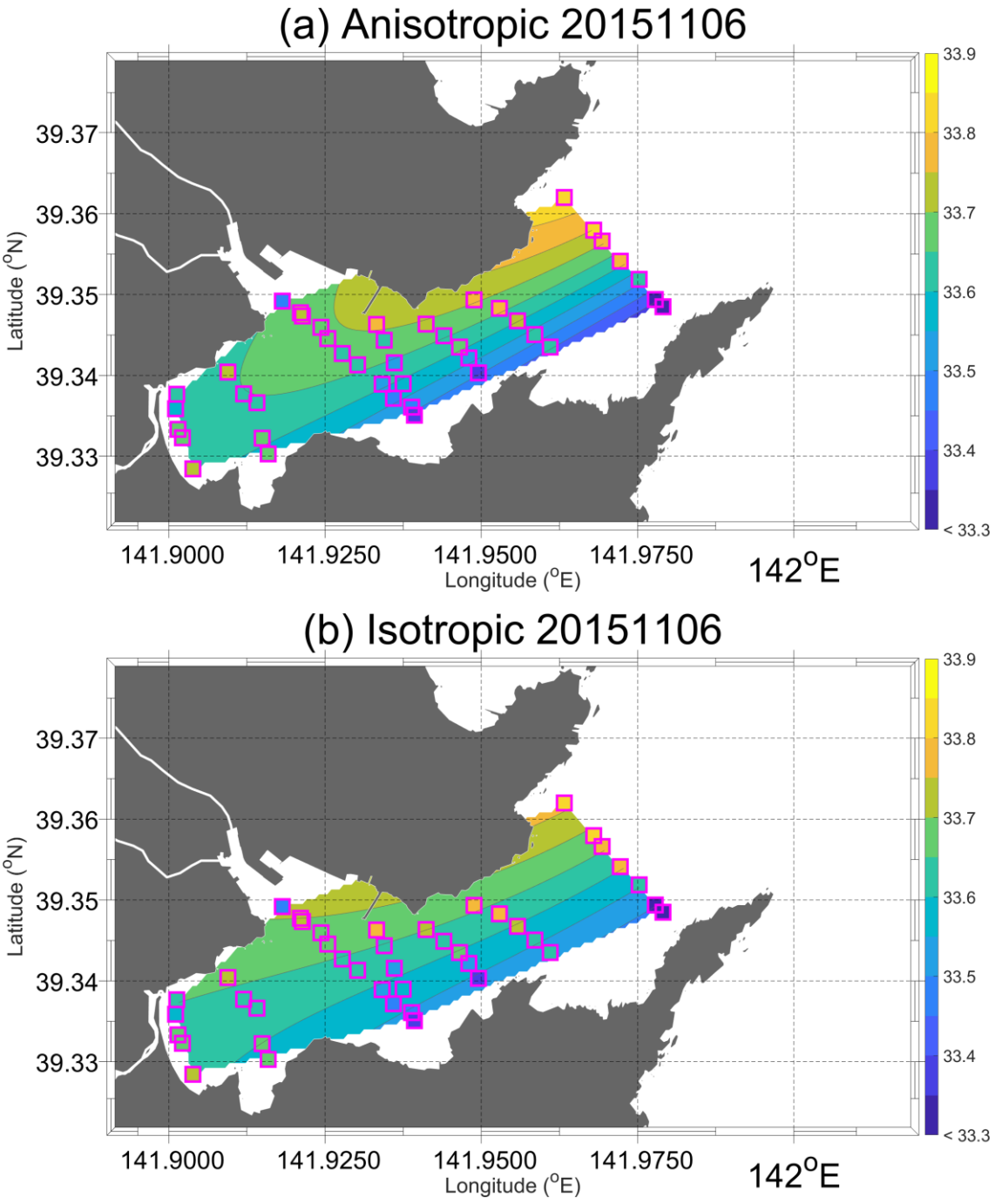

A.2.1-3-1, The objective analysis results of the positive salinity gradient pattern on November 6th, 2015 with (a) anisotropic method and (b) isotropic method. The colored magenta box indicates the observed sea surface salinity value before the objective analysis methods were applied.

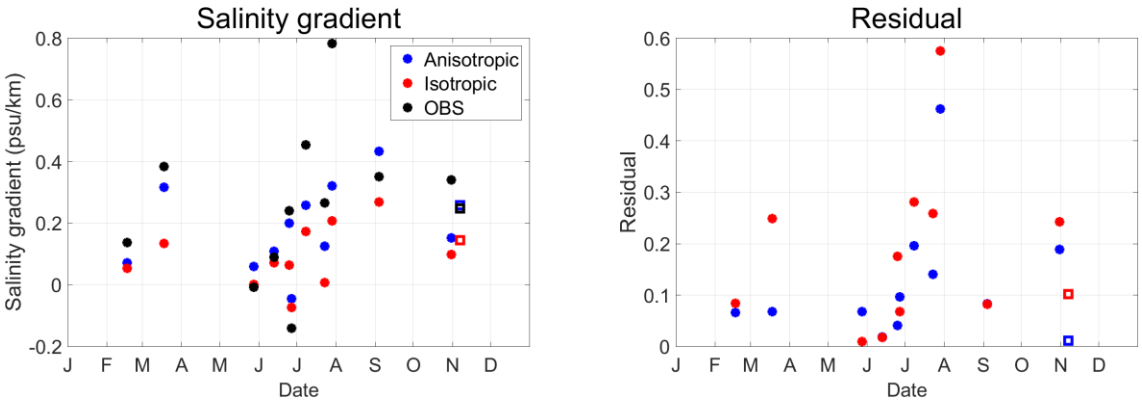

A.2.1-3-2, Salinity gradients by objective analysis methods from 2014 to 2015. Blue indicates the results of the anisotropic method, red indicates the results of the isotropic method and black indicates the gradient between the spatial averaged sea surface salinity in north stations (8, 9, 16, and 17 in Fig.2.1-1) and southern stations (11, 12, 13, and 14 in Fig.2.1-1). Squared-shaped dots are the value of the positive salinity gradient pattern on November 6th, 2015. The right panel shows residual between black and blue or red in the left panel, respectively.

A.2.2-1 Detailed algorisms for the estimation of time series of river discharge.

Based on the dataset that was produced by Adachi in 2013, who conducted observations of water levels continuously and flow velocities at intervals in Kozuchi river during a period from 2011 to 2013, we investigated the relationship with nearby precipitation data (Shinmachi station, Japan Meteorological Agency; Blue-star at Fig. 2.2-2).

According to lead-lag correlation analysis, it was found that precipitation on the previous day was highly correlated to the river discharge (Fig.A.2.2-1-1). This implies that variation in precipitation on the previous day leads to the variation in river discharge. As a next step, we estimated linear relationships between precipitation on the previous day and river discharge, which is

$$R_{first\ guess}(date) = \alpha P(date - 1) \quad \text{(A.2.2-1.1)}$$

where, $P(date - 1)$ indicates precipitation (mm d^{-1}) on the previous day and $R_{first\ guess}(date)$ indicates river discharge ($m^3\ s^{-1}$). The coefficients α were 0.4109 and 0.3480 for Otsuchi+Kozuchi River and Unosumai River, respectively. Fig.A.2.2-1-2 shows the scatter plot and estimated linear relationships of P, and $R_{\text{first guess}}$.

In addition to that, we considered the natural decrease of rivers after large precipitation by,

$$\begin{aligned} if \quad & R_{first\ guess}(date - 1) > R_{first\ gusee}(date), \\ R_{est}(date) &= \left(R_{first\ guess}(date - 1) + R_{first\ guess}(date)\right)/2 \\ else, \quad & R_{est}(date) = R_{first\ guess}(date). \end{aligned} \quad \text{(A.2.2-1.2)}$$

The comparison between the dataset that was produced by Adachi and the estimated river (R_{est}) is shown in Fig.A.2.2-1-3. Our estimated river tends to underestimate the dataset, especially, when river discharge is decreasing, but it has some meaning that only precipitation data were used for the estimation. The correlation between our estimated river discharge and the dataset was 0.64. It should be noted again that this estimation is based only on precipitation, i.e., the effects of groundwater or snow load were not considered.

The time series of daily river discharge in 2014 and 2015 were estimated by those algorisms with precipitation data in 2014 and 2015, which are shown in Fig.2.2-5.

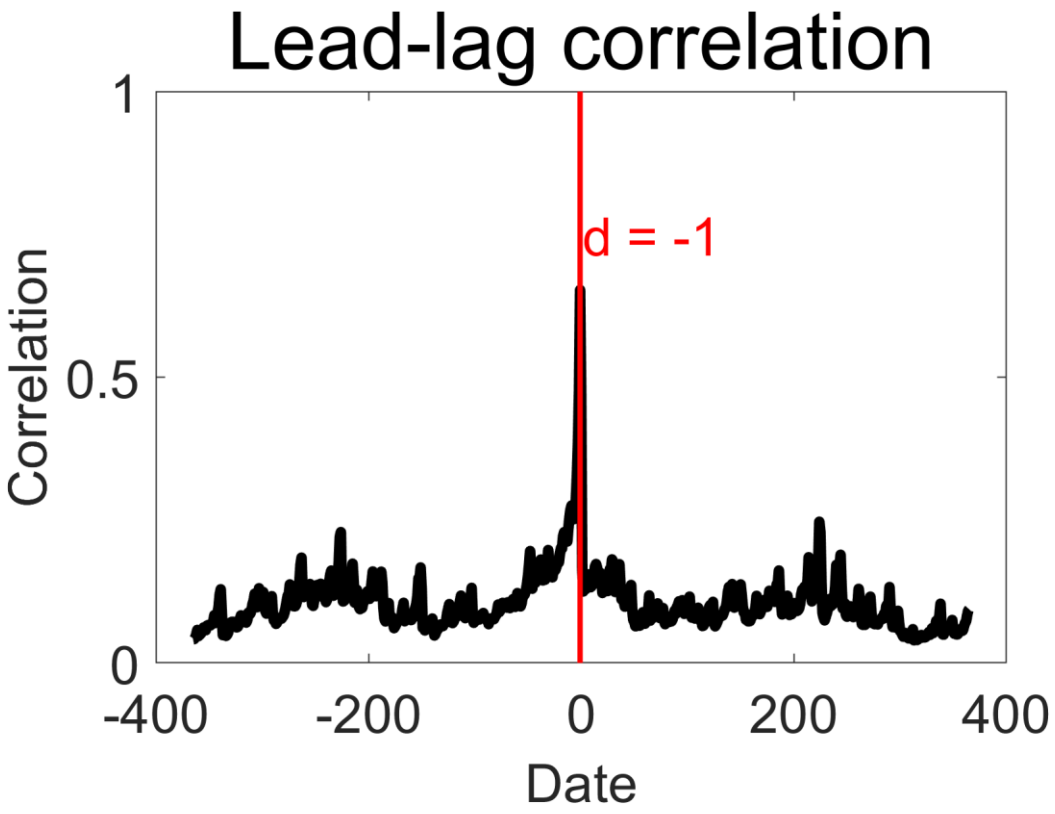

A.2.2-1-1, Lead-lag correlation between precipitation and river discharge from 2011 to 2013.

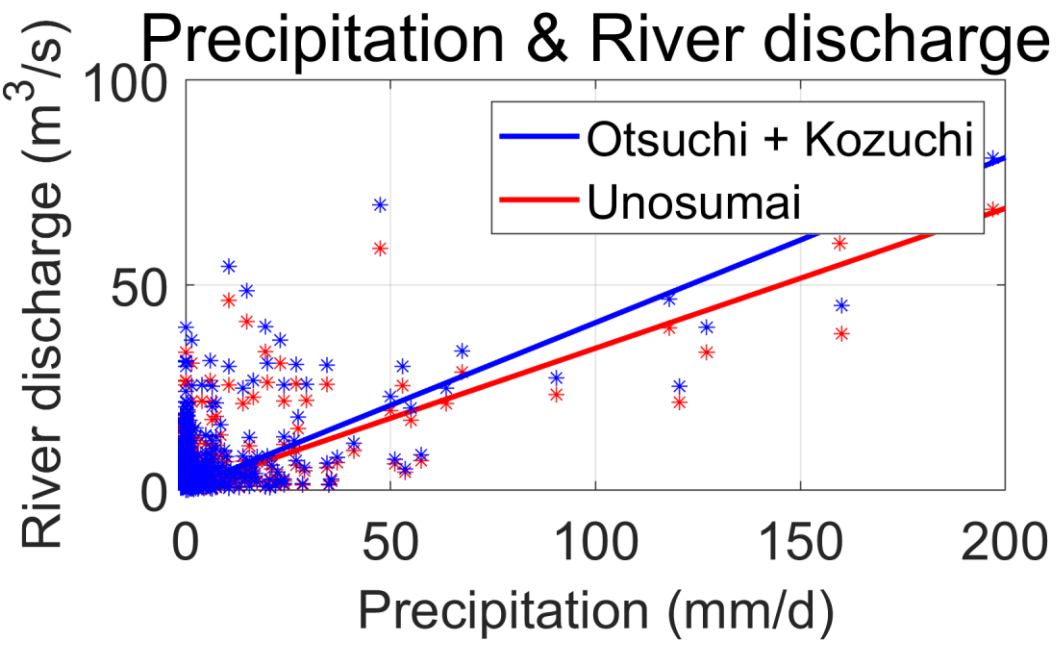

A.2.2-1-2, Relationship between precipitation and river discharge from 2011 to 2013. Blue and red color indicate Otsuchi+Kozuchi and Unosumai River, respectively.

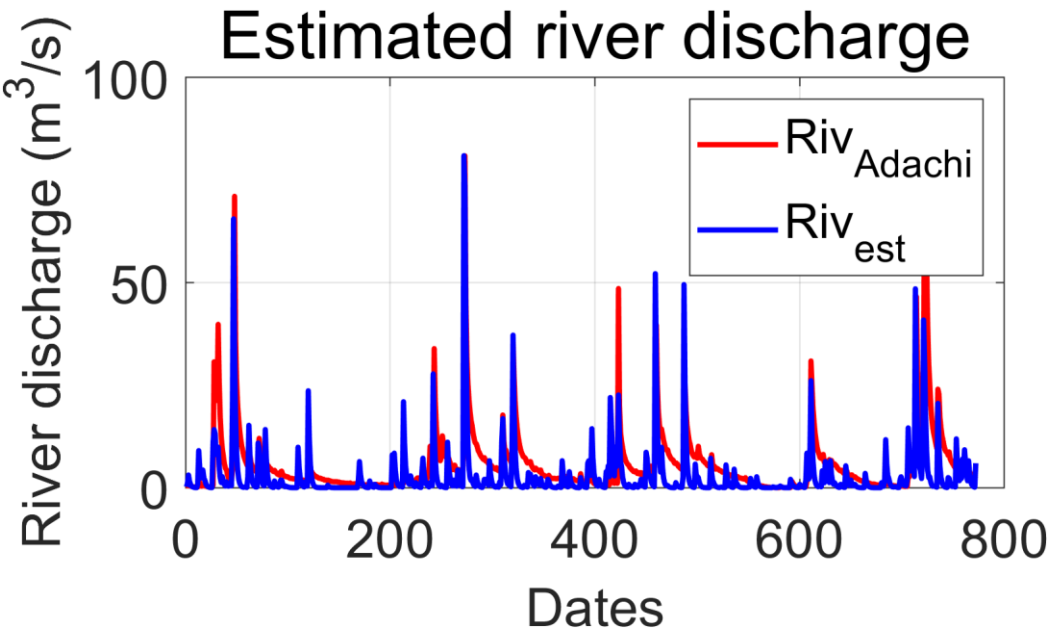

A.2.2-1-3, Comparison between estimated river discharge (blue) and dataset from 2011 to 2013.

A.2.2-2 Detailed converting processes from wind stress in Kamaishi to wind stress in Otsuchi.

Because of lack of observed data in Otsuchi Bay, wind stress in 2014 was converted from the wind data at Kamaishi station (Japan Meteorological Agency; magenta-triangle at Fig. 2.2-2), using relationships between wind data of the Otsuchi Bay and Kamashi in 2015. The relationships are estimated by wind stress in Kamaishi and Otsuchi in 2015, which are

$$Taux_o = \alpha_1 \, Taux_k + \alpha_2$$
$$Tauy_o = \alpha_3 \, Tauy_k + \alpha_4 \qquad \text{(A.2.2-2-1.1)}$$

where, subscripts o, and k indicate Otsuchi bay, and Kamaishi, respectively. The coefficients α_1, α_2, α_3, and α_4 are 3.470, 0.004, 3.534, and -0.002, respectively. Fig.A.2.2-2-1 shows the relationships. While zonal wind stress had a strong relationship, meridional wind stress had a weak relationship. However, the order of zonal wind stress was bigger than meridional wind stress.

The time series of daily zonal and meridional wind stress in 2014 were estimated by this procedure with wind data in Kamaichi in 2014, which are shown in Fig.2.2-6.

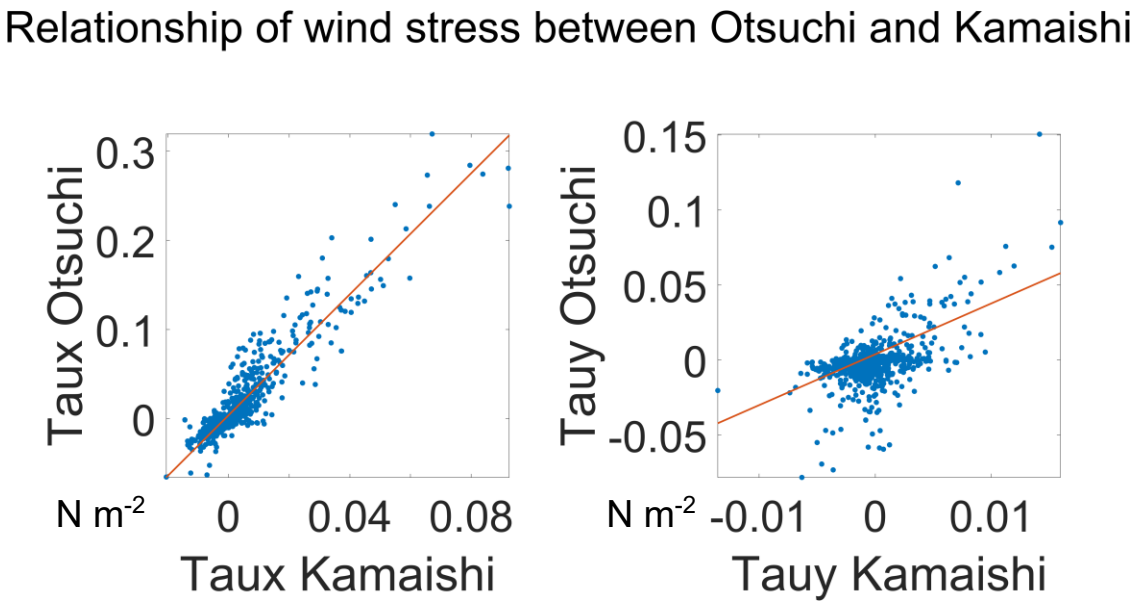

A.2.2-2-1, Relationship of wind stress between Otsuchi and Kamaishi in 2015.